Results in Physics 7 (2017) 288–309

Contents lists available at ScienceDirect

Results in Physics

journal homepage: www.journals.elsevier.com/results-in-physics

Analysis of heat transfer for unsteady MHD free convection flow of rotating Jeffrey nanofluid saturated in a porous medium

Nor Athirah Mohd Zin [a], Ilyas Khan [b,*], Sharidan Shafie [a], Ali Saleh Alshomrani [c]

[a] Department of Mathematical Sciences, Faculty of Science, Universiti Teknologi Malaysia, 81310 Johor Bahru, Malaysia
[b] Basic Sciences Department, College of Engineering Majmaah University, P.O. Box 66, Majmaah 11952, Saudi Arabia
[c] Department of Mathematics, Faculty of Science, King Abdul Aziz University, Jeddah, Saudi Arabia

ARTICLE INFO

Article history:
Received 26 November 2016
Received in revised form 18 December 2016
Accepted 23 December 2016
Available online 29 December 2016

Keywords:
Jeffrey nanofluid
AgNPs
MHD and Porosity
Rotating flow
Laplace transform technique

ABSTRACT

In this article, the influence of thermal radiation on unsteady magnetohydrodynamics (MHD) free convection flow of rotating Jeffrey nanofluid passing through a porous medium is studied. The silver nanoparticles (AgNPs) are dispersed in the Kerosene Oil (KO) which is chosen as conventional base fluid. Appropriate dimensionless variables are used and the system of equations is transformed into dimensionless form. The resulting problem is solved using the Laplace transform technique. The impact of pertinent parameters including volume fraction φ, material parameters of Jeffrey fluid λ_1, λ, rotation parameter r, Hartmann number Ha, permeability parameter K, Grashof number Gr, Prandtl number Pr, radiation parameter Rd and dimensionless time t on velocity and temperature profiles are presented graphically with comprehensive discussions. It is observed that, the rotation parameter, due to the Coriolis force, tends to decrease the primary velocity but reverse effect is observed in the secondary velocity. It is also observed that, the Lorentz force retards the fluid flow for both primary and secondary velocities. The expressions for skin friction and Nusselt number are also evaluated for different values of emerging parameters. A comparative study with the existing published work is provided in order to verify the present results. An excellent agreement is found.

Introduction

A nanofluid is a fluid containing nanometer-sized particles, called nanoparticles. Recently, nanofluid is regarded as one of the best heat transfer fluids. The term of nanofluid refers to a mixture of nanoparticles (e.g. carbon, metals and metal oxides) and an ordinary base fluid (e.g. water, ethylene glycol, lubricant oil and kerosene) which was first introduced by Choi and Eastman [1]. To meet the cooling rate requirement of industry, the conventional heat transfer fluids are not suitable and are found to have limited heat transfer capabilities due to their low thermal conductivity compared to metals. Therefore, nanoparticles are inserted to increase the thermal conductivities of the base fluids and this leads to an enhancement of the heat transfer. Looking into the above mentioned facts, many researchers have put their attentions in this subject including Mohyud-Din et al. [2,3], Haq et al. [4–6], Dinarvand et al. [7–10], Khan et al. [11–14] and Khan et al. [15]. In addition, Haq et al. [16] investigated numerically the effects of magnetohydrodynamics and volume fraction of carbon nanotubes (CNTs) on the flow and heat transfer in two lateral directions over a stretching sheet by using Runge-Kutta-Fehlberg with shooting technique. In a subsequent year, Haq et al. [17] discussed the convective heat transfer in MHD slip flow over a stretching surface in the presence of carbon nanotubes and solved numerically using shooting technique with a Runge-Kutta method. In another study, Haq et al. [18] presented the dual-nature solutions of the axisymmetric flow of a magneto-hydrodynamics nanofluid over a permeable shrinking sheet using same methodology as [17]. Besides that, some analytical studies of nanofluid between two concentric cylinders can be found in [19] and [20].

The study of rotating fluids has gained much interest nowadays since it has been encountered in many important problems such as cosmic and geophysical flows. The effect of Coriolis force helps us to understand the phenomena of earth's rotation, the behavior of ocean circulation and galaxies formation better. Therefore, many mathematical models including numerical and analytical studies are presented to study the effect of Coriolis force on the fluid flows. Saleem et al. [21] analyzed buoyancy and metallic particle effects on unsteady water-based fluid flow along a vertically rotating cone with the help of Runge-Kutta-Fehlberg method. Hosseini et al. [22] used Homotopy perturbation method to investigate nanofluid flow

* Corresponding author.
E-mail address: i.said@mu.edu.sa (I. Khan).

http://dx.doi.org/10.1016/j.rinp.2016.12.032
2211-3797/

and heat transfer between two horizontal plates in a rotating system. Sheikholeslami et al. [23] extended the idea of [22], by taking into account the magnetohydrodynamic (MHD) effect and solved the problem numerically using fourth-order Runge-Kutta method. Besides that, Hussain et al. [24] examined the flow and heat transfer effects of both single and multiple wall carbon nanotubes within the base fluid (water) in a rotating channel. In these papers, the authors have used the nanofluid model proposed by Tiwari and Das [25]. After that, Sheikholeslami and Ganji [26] extended the previous work of [23] and analyzed three dimensional nanofluid flow and heat transfer in a rotating system in the presence of magnetic field using Buongiorno's model [27]. Very recently, Khan et al. [28] studied numerically three dimensional squeezing flow of nanofluid in a rotating channel with lower stretching wall suspended by carbon nanotubes with the aid of Runge-Kutta-Fehlberg method. Few other attempts in this direction are those made by Nadeem et al. [29], Sree Ranga Vani and Prasada Rao [30], Das [31], Raza et al. [32], Mohyud-Din et al. [33] and Satya Narayana et al. [34].

Materials that do not obey the Newtonian law of viscosity are non-Newtonian fluids such as apple sauce, drilling muds, certain oils, ketchup and colloidal and suspension solution. The study of non-Newtonian fluids has gained interest because of their extensive industrial and technological applications. However, the Navier Stokes equations are no longer valid to precisely describe the rheological behavior of all non-Newtonian fluids. In view of their differences with Newtonian fluids, several models of non-Newtonian fluids have been proposed. The most common and simplest model of non-Newtonian fluids is Jeffrey fluid which has time derivative instead of convected derivative [35]. Hussain et al. [36] developed a model to examine the radiative hydromagnetic flow of Jeffrey nanofluid by an exponentially stretching sheet. Hayat et al. [37] investigated analytically three dimensional flow of Jeffrey nanofluid with a new mass flux condition using Homotopy analysis method.

Later on, Shehzad et al. [38,39], Hayat et al. [40], Dalir et al. [41] and Naramgari et al. [42] studied a magnetic field effect on the flow of Jeffrey nanofluid under various aspects. An analysis of the boundary layer flow and heat transfer in a Jeffrey fluid containing nanoparticles due to a stretchable cylinder was reported by Hayat et al. [43]. Nadeem and Saleem [44] presented the unsteady mixed convection flow on a rotating cone in a rotating Jeffrey nanofluid and solved analytically with the help of optimal homotopy analysis method. Very recently, Raju et al. [45] investigated numerically the influence of thermal radiation and chemical reaction on the boundary layer flow of a magnetohydrodynamic Jeffrey nanofluid over a permeable cone in the presence of thermophoresis and Brownian effects using Runge-Kutta fourth order with shooting technique. Also, some important articles investigated on peristaltic flow of Jeffrey nanofluid are well documented in [46–49].

The current study is mainly focused on the unsteady MHD free convection flow of rotating Jeffrey nanofluid past an infinite vertical disk saturated in a porous medium. To the best of our knowledge, most of the previous studies on Jeffrey nanofluid have applied the Buongiorno's model [27] and no study utilizing the Tiwari and Das model has been reported [25]. Therefore, in this present study, the nanofluid model proposed by Tiwari and Das [25] is used to study Jeffrey nanofluid. An analytical technique called Laplace transform method is implemented to the governing equations. Results for velocity and temperature profiles for various pertinent parameters are plotted graphically and discussed in details. A comparative study is also provided in sense of limiting cases for verification and an excellent agreement is found. Numerical results for skin friction and Nusselt number are evaluated and presented in tables.

Mathematical formulation

Consider the unsteady MHD free convection flow of an incompressible Jeffrey nanofluid saturated in porous medium past an infinite vertical plate. A coordinate frame is chosen in which the x-axis is taken vertically upwards along the plate, while the z-axis is measured perpendicular to it. The plate is embedded in a nanofluid consisting of Kerosene oil (base fluid) and Silver nanoparticles (AgNPs). Consider the fluid is in a rigid body rotation with a constant angular velocity, Ω about the z-axis as shown in Fig. 1.

A uniform magnetic field of strength B_0 is imposed normal to the x-axis. Induced magnetic field is considered negligible for a small magnetic Reynolds number compared to the applied magnetic field [50]. It is also assumed that the external electric field and electric field are neglected due to the no polarization and voltage exists [51–53]. Initially, both the plate and fluid are at rest with a constant temperature, T_∞. At time $t > 0$, the temperature is raised or lowered to T_w which is thereafter maintained constant.

Under the above assumptions, applying the usual Boussinesq approximation [54] and using the nanofluid model proposed by Tiwari and Das [25], the momentum and energy equations for unsteady MHD free convection flow of rotating Jeffrey nanofluid in the presence of thermal radiation are governed by:

$$\rho_{nf}\left(\frac{\partial F}{\partial t}+2\Omega i F\right)=\frac{\mu_{nf}}{1+\lambda_1}\left(1+\lambda_2\frac{\partial}{\partial t}\right)\frac{\partial^2 F}{\partial z^2}-\frac{\mu_{nf}\phi_1}{k^*(1+\lambda_1)}\left(1+\lambda_2\frac{\partial}{\partial t}\right)F-\sigma B_0^2 F+(\rho\beta_T)_{nf}g(T-T_\infty), \tag{1}$$

$$(\rho c_p)_{nf}\frac{\partial T}{\partial t}=k_{nf}\frac{\partial^2 T}{\partial z^2}-\frac{\partial q_r}{\partial z}. \tag{2}$$

The initial and boundary conditions are taken to be:

$$F(y,0)=0,\quad T(y,0)=T_\infty, \tag{3}$$

$$F(0,t)=0,\quad T(0,t)=T_w, \tag{4}$$

$$F(\infty,t)=0,\quad T(\infty,t)=T_\infty. \tag{5}$$

Here $F=u+iv$ are complex velocity where u and v are real and imaginary part respectively, ρ_{nf} is the density of nanofluids, μ_{nf} is the dynamic viscosity of nanofluid, $\lambda_{i=1,2}$ are the material parameters of Jeffrey fluid, ϕ_1 is the porosity, k^* is the permeability of the porous medium, σ is the electric conductivity, $(\rho\beta_T)_{nf}$ is the thermal expansion coefficient of nanofluid, g is the acceleration due to gravity, T is the temperature, $(\rho c_p)_{nf}$ is the heat capacitance of the nanofluid, k_{nf} is the thermal conductivity of nanofluid and q_r is the radiative heat flux. Note that the two fluid models, namely viscous nanofluid model and second grade nanofluid model can be obtained as special cases from the present Jeffrey nanofluid model by taking $\lambda_1=\lambda_2=0$, respectively $\lambda_1=0$, as it will lead to the expression of second grade nanofluid.

Following [55–59], the relations of ρ_{nf}, μ_{nf}, $(\rho\beta_T)_{nf}$, $(\rho c_p)_{nf}$ and k_{nf} are given as:

$$\rho_{nf}=(1-\varphi)\rho_f+\varphi\rho_s, \tag{6}$$

$$\mu_{nf}=\frac{\mu_f}{(1-\varphi)^{2.5}}, \tag{7}$$

$$(\rho\beta)_{nf}=(1-\varphi)(\rho\beta)_f+\varphi(\rho\beta)_s, \tag{8}$$

$$(\rho c_p)_{nf}=(1-\varphi)(\rho c_p)_f+\varphi(\rho c_p)_s, \tag{9}$$

$$\frac{k_{nf}}{k_f}=\frac{k_s+2k_f-2\varphi(k_f-k_s)}{k_s+2k_f+\varphi(k_f-k_s)}. \tag{10}$$

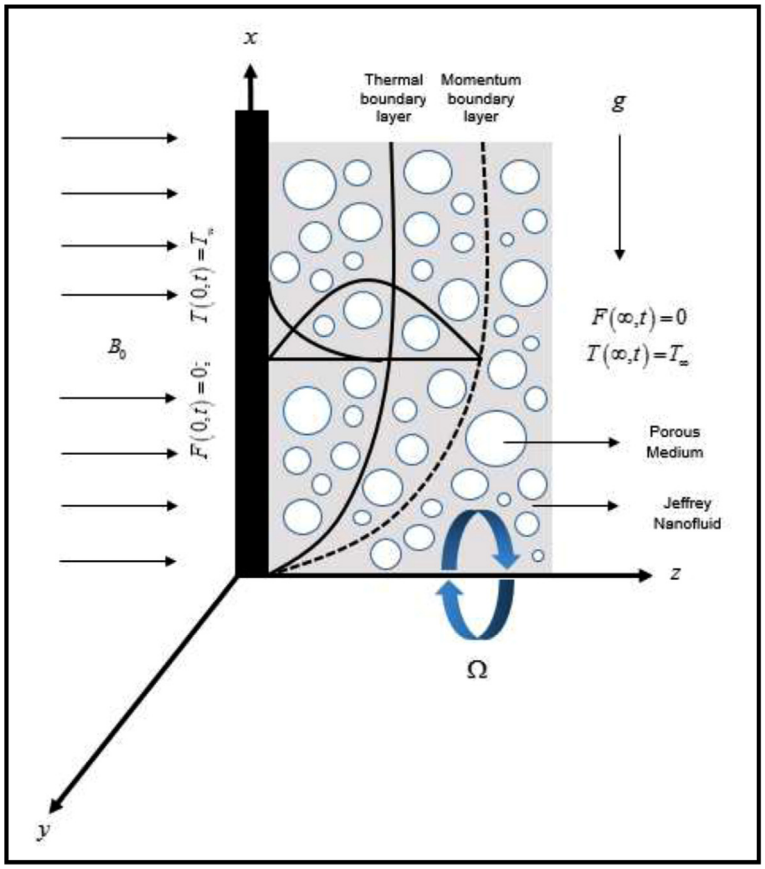

Fig. 1. Physical model of rotating Jeffrey nanofluid saturated in porous medium.

In which φ is the nanoparticles volume fraction, ρ_f is the density of base fluid, ρ_s is the density of solid nanoparticles, μ_f is the dynamic viscosity of the base fluid, β_f is the volumetric coefficient of thermal expansions of base fluid, β_s is the volumetric coefficient of thermal expansions of solid nanoparticles, $(c_p)_f$ and $(c_p)_s$ are the specific heat of capacities of base fluids and solid nanoparticles at constant pressure and k_f and k_s are the thermal conductivities of the base fluid and solid nanoparticles respectively. According to Turkyilmazoglu and Pop [60], the expressions given in (6)–(10) are restricted to spherical nanoparticles. The thermophysical properties of base fluids and nanoparticles are given in Table 1.

Using Rosseland approximation, the radiation heat flux [61–63] leads to

$$q_r = -\frac{4\sigma^*}{3k_1}\frac{\partial T^4}{\partial y}, \tag{11}$$

where σ^* is the Stefan-Boltzman constant and k_1 is the absorption coefficient. Further, we assume the temperature differences within the flow are sufficiently small such that T^4 is a linear temperature function which is expanded by Taylor series expansion about T_∞. Neglecting the higher order term gives

$$T^4 \approx 4T_\infty^3 T - 3T_\infty^4. \tag{12}$$

Upon substituting Eqs. (11) and (12) into (2), reduces to

$$\frac{\partial T}{\partial t} = \frac{k_f}{(\rho c_p)_{nf}}\left(\frac{k_{nf}}{k_f} + \frac{16\sigma^* T_\infty^3}{3k_f k_1}\right)\frac{\partial^2 T}{\partial z^2}. \tag{13}$$

Introducing the following dimensionless variables

$$F^* = \frac{F}{U_0},\ z^* = \frac{zU_0}{\upsilon},\ t^* = \frac{tU_0^2}{\upsilon},\ \theta = \frac{T-T_\infty}{T_w - T_\infty}. \tag{14}$$

Employing the dimensionless variables defined in (14) into Eqs. (1) and (13) along with initial and boundary conditions (3)–(5) leads to the expressions of non-dimensional form (drop out the star notation for simplicity)

$$\frac{\partial F}{\partial t} + 2irF = \frac{a_1}{1+\lambda_1}\left(1+\lambda\frac{\partial}{\partial t}\right)\frac{\partial^2 F}{\partial z^2} - \frac{a_1}{K(1+\lambda_1)}\left(1+\lambda\frac{\partial}{\partial t}\right)F - \left(\frac{Ha}{a_3}\right)F + a_2 Gr\theta, \tag{15}$$

Table 1
Thermophysical properties of different base fluids and nanoparticles [67–69].

Physical properties	Base fluids			Nanoparticles	
	Water	Kerosene	Ethylene glycol	Cu	Ag
ρ (kg/m^3)	997.1	780	1115	8933	10500
c_p (J/kg K)	4179	2090	2386	385	235
k (W/m K)	0.613	0.149	0.2499	401	429
β (K^{-1})	21×10^{-5}	9.9×10^{-4}	3.41×10^{-3}	1.67×10^{-5}	1.89×10^{-5}
Pr	6.2	21	203	–	–

$$\frac{\partial\theta}{\partial t}=a_4\frac{\partial^2\theta}{\partial z^2}, \tag{16}$$

subjected to initial and boundary conditions

$$F(z,0)=0,\ \theta(z,0)=0,\ z>0, \tag{17}$$

$$F(0,t)=0,\ \theta(0,t)=1,\ t>0, \tag{18}$$

$$F(\infty,t)=0,\ \theta(\infty,t)=0,\ t>0. \tag{19}$$

Here r is the rotation parameter, λ is the dimensionless material parameter, K is the permeability parameter, Ha is the Hartmann number or magnetic parameter, Gr is the Grashof number which is defined as:

$$r=\frac{\Omega\upsilon}{U_0^2},\ \lambda=\frac{\lambda_2U_0^2}{\upsilon},\ \frac{1}{K}=\frac{\phi_1\upsilon}{k^*U_0^2},\ Ha=\frac{\sigma B_0^2\upsilon}{\rho U_0^2},\ Gr=\frac{g\beta\upsilon(T_w-T_\infty)}{U_0^3}, \tag{20}$$

with

$$a_1=\frac{1}{(1-\varphi)^{2.5}\left\{(1-\varphi)+\varphi\frac{\rho_s}{\rho_f}\right\}},\ a_2=\frac{(1-\varphi)\rho_f+\varphi\frac{\beta_s}{\beta_f}}{\rho_{nf}},$$
$$a_3=(1-\varphi)+\varphi\frac{\rho_s}{\rho_f},\ a_4=\frac{1}{m_{11}Pr}(m_{12}+Rd),$$
$$m_1=(1-\varphi)+\varphi\frac{(\rho c_p)_s}{(\rho c_p)_f},\ m_2=\frac{k_s+2k_f-2\varphi(k_f-k_s)}{k_s+2k_f+\varphi(k_f-k_s)}, \tag{21}$$

where

$$Pr=\frac{\upsilon_f}{\alpha_f},\ Rd=\frac{16}{3}\frac{\sigma^*T_\infty^3}{k_fk_1}, \tag{22}$$

are Prandtl number and radiation parameter, respectively.

Solution of the problem

In order to proceed for the solution of the above problem, we use the Laplace transform technique. Thus, by taking the Laplace transform of Eqs. (15) and (16) together with the initial and boundary conditions (17)–(19), takes the form

$$\frac{d^2\bar F(z,q)}{dz^2}-\left(\frac{b_4+b_1q}{b_2+b_3q}\right)\bar F(z,q)=-\frac{a_2Gr}{b_2+b_3q}\bar\theta(z,q), \tag{23}$$

$$\frac{d^2\bar\theta(z,q)}{dz^2}-\frac{1}{a_4}q\bar\theta(z,q)=0, \tag{24}$$

$$\bar F(0,q)=0,\ \bar F(\infty,q)=0, \tag{25}$$

$$\bar\theta(0,q)=\frac{1}{q},\ \bar\theta(\infty,q)=0, \tag{26}$$

in which $\bar F(z,q)$ and $\bar\theta(z,q)$ indicate the Laplace transform of $F(z,t)$ and $\theta(z,t)$ respectively, and the arbitrary constants are given as

$$b_1=1+\frac{a_1\lambda}{K(1+\lambda_1)},\ b_2=\frac{a_1}{1+\lambda_1},\ b_3=\frac{a_1\lambda}{1+\lambda_1},$$
$$b_4=\frac{Ha}{a_3}+\frac{a_1}{K(1+\lambda_1)}+2ir. \tag{27}$$

Using (26) into (24) leads to the expression

$$\bar\theta(z,q)=\frac{1}{q}\exp\left(-z\sqrt{\frac{q}{a_4}}\right). \tag{28}$$

Taking the inverse Laplace transform of Eq. (28), the solution for temperature distribution is obtained as

$$\theta(z,t)=erfc\left(\frac{z}{2\sqrt{a_4t}}\right), \tag{29}$$

where $erfc(\cdot)$ being the complimentary error function. Meanwhile, substituting Eqs. (28) into (23) and making use of (25) gives

$$\bar F(z,q)=d_1[\bar F_1(q).\bar F_2(z,q)], \tag{30}$$

where

$$\bar F_1(q)=\frac{1}{(q+d_2)^2-d_3^2}, \tag{31}$$

$$\bar F_2(z,q)=\frac{1}{q}\exp\left(-z\sqrt{\frac{b_4+b_1q}{b_2+b_3q}}\right)-\frac{1}{q}\exp\left(-z\sqrt{\frac{q}{a_4}}\right). \tag{32}$$

Inversion Laplace transform of (31) yields the expression

$$F_1(t)=\frac{1}{d_{13}}\exp(-d_{12}t)\sinh(d_{13}t), \tag{33}$$

where

$$d_1=\frac{a_2a_4Gr}{b_3},\ d_2=\frac{b_2-a_4b_1}{2b_3},\ d_3=\frac{\sqrt{(b_2-a_4b_1)^2+4a_4b_3b_4}}{2b_3}. \tag{34}$$

In order to find the inverse Laplace of Eq. (32), we arrange it in the form

$$\bar F_2(z,q)=\bar A_1(z,q)-\bar A_2(z,q), \tag{35}$$

where

$$\bar A_1(z,q)=\frac{1}{q}\exp\left(-z\sqrt{\frac{b_4+b_1q}{b_2+b_3q}}\right), \tag{36}$$

$$\bar A_2(z,q)=\frac{1}{q}\exp\left(-z\sqrt{\frac{q}{a_4}}\right). \tag{37}$$

In order to find the inverse Laplace transform of Eq. (36), we split (36) in the following form

$$\bar G_1(q)=\frac{1}{q}, \tag{38}$$

$$\bar G_2(z,q)=\exp\left(-z\sqrt{\frac{b_4+b_1q}{b_2+b_3q}}\right). \tag{39}$$

Taking the inverse Laplace transform of Eq. (38) and using the inversion formula of compound function of Eq. (39) implies

$$G_1(t)=1, \tag{40}$$

$$G_2(z,t)=\delta(t)e^{-z\sqrt{L_2}}+\int_0^\infty\frac{z}{2h\sqrt{\pi}}\sqrt{\frac{L_3}{t}}e^{-\frac{z^2}{4h}-L_1t-hL_2}.I_1(2\sqrt{L_3ht})dh, \tag{41}$$

with

$$L_1=\frac{b_2}{b_3},\ L_2=\frac{b_1}{b_3},\ L_3=\frac{b_1L_1-b_4}{b_3}, \tag{42}$$

where $I_1(\cdot)$ is modified Bessel function of the first kind of order. Since $\bar A_1(z,q)$ involves two multiplication of functions (38) and (39), therefore we have to use the convolution theorem, hence

$$A_1(z,t)=\int_0^t G_1(t-s).G_2(z,s)ds$$
$$=e^{-z\sqrt{L_2}}+\frac{1}{2}\sqrt{\frac{L_3}{\pi}}\int_0^t\int_0^\infty\frac{z}{h\sqrt{s}}e^{-\frac{z^2}{4h}-L_1s-hL_2}.I_1(2\sqrt{L_3hs})dhds. \tag{43}$$

Besides that, the inverse Laplace of Eq. (37) is given by

$$A_2(z,t) = erfc(\frac{z}{2\sqrt{a_4 t}}). \tag{44}$$

Then,

$$F_2(z,t) = e^{-z\sqrt{L_2}} + \frac{1}{2}\sqrt{\frac{L_3}{\pi}}\int_0^t \int_0^\infty \frac{z}{h\sqrt{s}} e^{-\frac{z^2}{4h} - L_1 s - hL_2} . I_1(2\sqrt{L_3 hs}) dhds. \tag{45}$$

Finally, using the convolution theorem again, the solution of velocity profile of Eq. (30) can be expressed as:

$$\begin{aligned} F(z,t) = {} & \frac{d_1}{d_3}\int_0^t e^{-d_2(t-l)-z\sqrt{L_2}} \sinh[d_3(t-l)]dl + \frac{d_1}{d_3}\frac{1}{2}\sqrt{\frac{L_3}{\pi}}\int_0^t \int_0^l \int_0^\infty \\ & \times \frac{z}{h\sqrt{s}} e^{-d_2(t-l)-\frac{z^2}{4h}-L_1 s - hL_2} \sinh[d_3(t-l)] I_1(2\sqrt{L_3 hs}) dhdsdl \\ & - \frac{d_1}{d_3}\int_0^t e^{-d_2(t-l)} \sinh[d_3(t-l)] erfc\left(\frac{z}{2\sqrt{a_4 l}}\right) dl. \end{aligned} \tag{46}$$

Skin friction and Nusselt number

The dimensionless skin friction, τ for rotating flow of Jeffrey nanofluid is defined as

$$\tau = \frac{1}{1+\lambda_1}\left(1 + \lambda\frac{\partial}{\partial t}\right)\frac{\partial F}{\partial z}\Big|_{z=0}. \tag{47}$$

Thus,

$$\begin{aligned} \tau(t) = {} & \frac{d_1}{1+\lambda_1}\int_0^t e^{d_2(l-t)}\left[\frac{1}{\sqrt{\pi a_4 l}} - \sqrt{L_2}\right]\left\{\frac{(1-\lambda d_2)}{d_3}\sinh[d_3(t-l)]\right. \\ & \left. + \lambda\cosh[d_3(t-l)]\right\}dl \quad + \frac{d_1}{1+\lambda_1}\frac{1}{2}\sqrt{\frac{L_3}{\pi}}\int_0^t \int_0^l \int_0^\infty \\ & \times \frac{1}{h\sqrt{s}} e^{-L_1 s - hL_2 + d_2(l-t)} I_1(2\sqrt{L_3 hs}) \\ & \times \left\{\frac{(1-\lambda d_2)}{d_3}\sinh[d_3(t-l)] + \lambda\cosh[d_3(t-l)]\right\} dhdsdl. \end{aligned} \tag{48}$$

The rate of heat transfer is given in the form of Nusselt number as:

$$Nu = -\frac{\partial\theta}{\partial t}\Big|_{z=0} = \frac{1}{\sqrt{\pi a_4 t}}. \tag{49}$$

Limiting cases

In order to highlight the theoretical value of the general solutions obtained in (29) and (46) for temperature and velocity as well as to gain physical regime, we consider two special cases by taking suitable parameters equal to zero.

Case 1: Absence of rotation, MHD, radiation and porosity

By making radiation parameter, $Rd = 0$ the obtained temperature (29) implies

$$\theta(z,t) = erfc\left(\frac{z}{2}\sqrt{\frac{m_1 Pr}{m_2 t}}\right). \tag{50}$$

Furthermore, by putting $r = Ha = Rd = 0$ and $K \to \infty$ in Eq. (46), reduces the obtained velocity profile to

$$\begin{aligned} F(z,t) = {} & \frac{d_1}{d_{12}}\int_0^t e^{-d_{12}(t-l)-z\sqrt{L_{12}}} \sinh[d_{12}(t-l)]dl + \frac{d_1}{d_{12}}\frac{1}{2}\sqrt{\frac{L_{13}}{\pi}}\int_0^t \int_0^l \int_0^\infty \\ & \times \frac{z}{h\sqrt{s}} e^{-d_{12}(t-l)-\frac{z^2}{4h}-L_1 s - hL_{12}} \sinh[d_{12}(t-l)] I_1(2\sqrt{L_{13} hs}) dhdsdl \\ & - \frac{d_1}{d_{12}}\int_0^t e^{-d_{12}(t-l)} \sinh[d_{12}(t-l)] erfc\left(\frac{z}{2\sqrt{a_{14} l}}\right) dl, \end{aligned} \tag{51}$$

where

$$a_{14} = \frac{m_2}{m_1 Pr},\ d_{12} = \frac{b_2 - a_4}{2b_3},\ L_{12} = \frac{1}{b_3},\ L_{13} = \frac{L_1}{b_3}. \tag{52}$$

It is noted that, by taking volume fraction, $\varphi = 0$ in Eqs. (50) and (51), these solutions will be reduced to the regular Jeffrey fluid which is identical to the solution obtained by Khan [64] in Eqs. (18) and (31) (See Figs. 2 and 3).

Case 2: Solution in the absence of λ_1

Interestingly, the solution of Eq. (46) can be reduced to rotating second grade fluid with the porosity, MHD and radiation effects if $\lambda_1 = 0$.

$$\begin{aligned} F(z,t) = {} & \frac{d_{21}}{d_{23}}\int_0^t e^{-d_{22}(t-l)-z\sqrt{L_{22}}} \sinh[d_{23}(t-l)]dl + \frac{d_{21}}{d_{23}}\frac{1}{2}\sqrt{\frac{L_{23}}{\pi}}\int_0^t \int_0^l \int_0^\infty \\ & \times \frac{z}{h\sqrt{s}} e^{-d_{22}(t-l)-\frac{z^2}{4h}-\frac{s}{\lambda}-hL_{22}} \sinh[d_{23}(t-l)] I_1(2\sqrt{L_{23} hs}) dhdsdl \\ & - \frac{d_{21}}{d_{23}}\int_0^t e^{-d_{22}(t-l)} \sinh[d_{23}(t-l)] erfc\left(\frac{z}{2\sqrt{a_4 l}}\right) dl, \end{aligned} \tag{53}$$

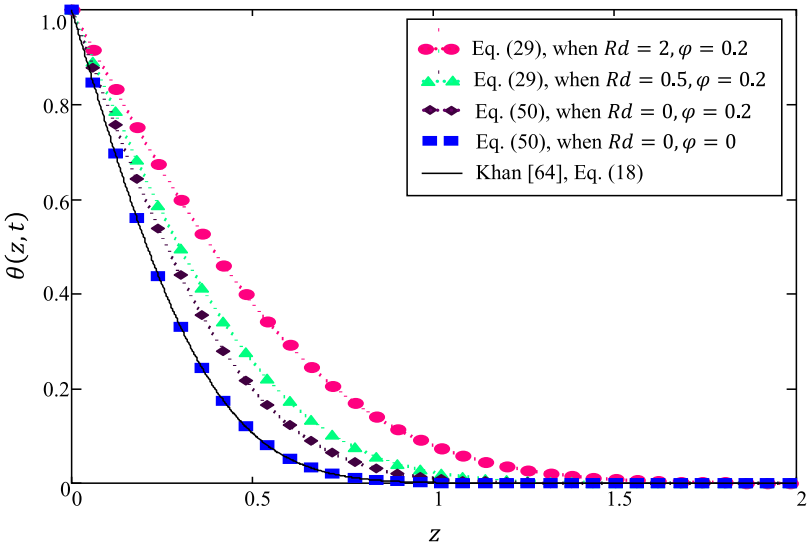

Fig. 2. Comparison of temperature $\theta(z,t)$ in (50) with (18) obtained by Khan [64] when $Pr = 21$ and $t = 1$.

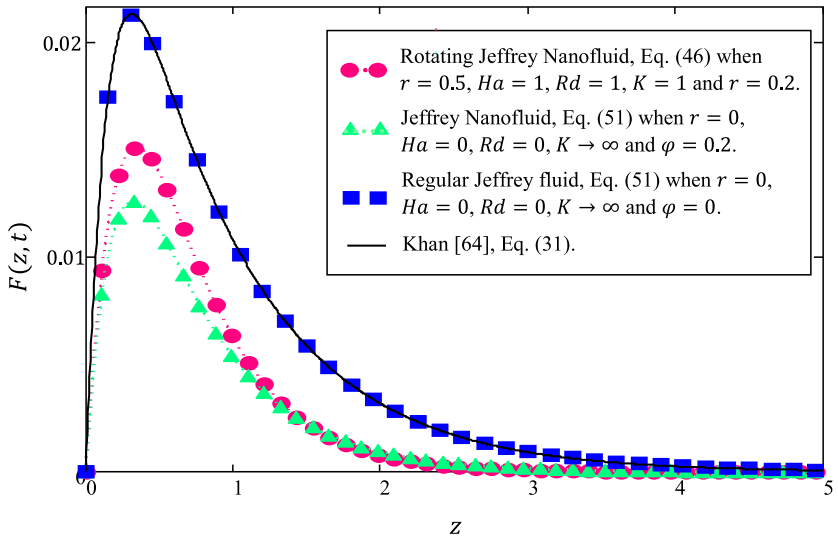

Fig. 3. Comparison of velocity $F(z,t)$ in (51) with (31) obtained by Khan [64] when $\lambda_1 = \lambda = 1$, $Gr = 1$, $Pr = 21$ and $t = 1$.

where

$$b_{21} = 1 + \frac{a_1\lambda}{K},\ b_{24} = \frac{Ha}{a_3} + \frac{a_1}{K} + 2ir, d_{21} = \frac{a_2 a_4 Gr}{a_1\lambda},$$
$$d_{22} = \frac{a_1 - a_4 b_{21}}{2a_1\lambda},\ d_{23} = \frac{\sqrt{(a_1 - a_4 b_{21})^2 + 4\lambda a_1 a_4 b_{24}}}{2\lambda a_1},$$
$$L_{22} = \frac{1}{a_1\lambda} + \frac{1}{K},\ L_{23} = \frac{1}{a_1\lambda^2} + \frac{1}{K\lambda} - \frac{b_4}{a_1\lambda}. \tag{54}$$

However, by taking $r = 0$, $Ha = 0$, $Rd = 0$ and $K \to \infty$ into Eq. (53), it will be reduced to

$$F(z,t) = \frac{d_{31}}{d_{32}}\int_0^t e^{d_{32}(l-t) - \frac{z}{\sqrt{a_1\lambda}}}\sinh[d_{32}(t-l)]dl + \frac{d_{31}}{d_{32}}\frac{1}{2\lambda\sqrt{a_1\pi}}\int_0^t\int_0^l\int_0^\infty \times \frac{z}{h\sqrt{s}} e^{d_{32}(l-t) - \frac{z^2}{4h} - \frac{1}{\lambda}\left(s + \frac{h}{a_1}\right)}\sinh[d_{32}(t-l)]I_1\left(\frac{2}{\lambda}\sqrt{\frac{hs}{a_1}}\right)dhdsdl - \frac{d_{31}}{d_{32}}\int_0^t e^{d_{32}(l-t)}\sinh[d_{32}(t-l)]erfc\left(\frac{z}{2}\sqrt{\frac{m_{11}Pr}{m_{12}l}}\right)dl. \tag{55}$$

In which

$$d_{31} = \frac{a_2 m_{12} Gr}{a_1\lambda m_{11} Pr},\ d_{32} = \frac{a_1 m_{11} Pr - m_{12}}{2a_1\lambda m_{11} Pr}. \tag{56}$$

Eq. (55) is satisfactorily identical to the published results obtained by Samiulhaq et al. [65] in Eq. (11) when $\varphi = 0$ and $Gr = 1$. Furthermore, clearly Fig. 4 shows that the graph of Eq. (55) matches well with Eq. (11) in Samiulhaq et al. [65] when the volume fraction of nanoparticles is neglected. An excellent agreement is noted.

Result and discussion

This section is prepared to study the impact of pertinent parameters namely volume fraction φ, material parameter λ_1, dimensionless material parameter λ, Hartmann number or magnetic parameter Ha, rotation parameter r, permeability parameter K, Grashof number Gr, Prandtl number Pr, radiation parameter Rd and dimensionless time t on velocity field components and temperature distributions which are displayed graphically in

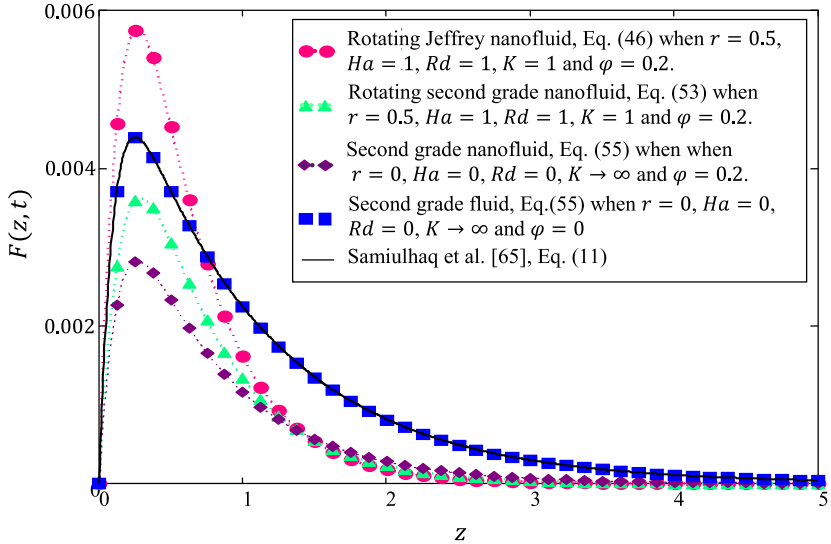

Fig. 4. Comparison of velocity $F(z,t)$ in (55) with (11) obtained by Samiulhaq et al. [65] when $\lambda_1 = \lambda = 0.8$, $Gr = 1$, $Pr = 21$ and $t = 0.5$.

Figs. 5–23. Kerosene oil is chosen as a conventional base fluid with silver (Ag) nanoparticles. The panels (a) and (b) in each plot indicate the variations of real and imaginary part of velocity and are also called as primary and secondary velocity, respectively.

Figs. 5a and 5b show a graphical description of the fluid flow for two types of nanoparticles namely copper nanoparticles (CuNPs) and AgNPs. Obviously, from this figure AgNPs have slightly higher velocity compared to CuNPs. This shows that, the viscosity and thermal conductivity of CuNPs are greater compared to AgNPs. Besides that, AgNPs also seem to have smallest hydrodynamics.

Figs. 6a and 6b depict the variation in velocity due to increment in nanoparticle volume fraction for AgNPs. It is observed that an increase in the amount of volume fraction decreases the velocity profile. This is due to the reason that the presence of solid nanoparticles leads to further thinning of the velocity boundary layer thickness and hence slows down the fluid motion.

Figs. 7a and 7b are plotted in order to show the impact of different types of base fluid (water, Kerosene and Ethylene glycols) on velocity profile. Clearly, water has the highest velocity followed by Kerosene and Ethylene glycols which means it has the lowest viscosity compared to other base fluids for both real and imaginary parts of velocity.

The behaviors of material parameter of Jeffrey fluid, λ_1 (when λ is fixed) on velocity fields are portrayed in Figs. 8a and 8b. As λ_1 increases, the primary and secondary velocities decrease. However, a quite opposite trend is noticed for dimensionless material parameter of Jeffrey fluid, λ as pointed out in Figs. 9a and 9b. It can be observed that an increase of λ tends to decrease the velocities for both primary and secondary profiles. Physically, this is because λ is a viscoelastic parameter and viscoelasticity is a property of combined material exhibiting both elastic and viscous behavior when undergoing deformation. Hence, an increase of viscosity and elasticity will always retard the fluid flow [66]. Besides that, similar patterns are observed in Figs. 10a and 10b when both parameters are assumed to have same values.

Furthermore, the influences of rotation parameter, r on velocity components are demonstrated in Figs. 11a and 11b. Here, clearly, the rotation effects retard the fluid flow in primary flow direction in Fig. 11a, and the opposite trend is noticed in the secondary flow direction as shown in Fig. 11b. The velocity profile in secondary flow direction accelerates as r increases in the region near the plate, and later reduces in the region away from the plate due to the fact that Coriolis force is dominant in the region near to the axis of rotation. Besides that, from Fig. 11b we notice that the effect of

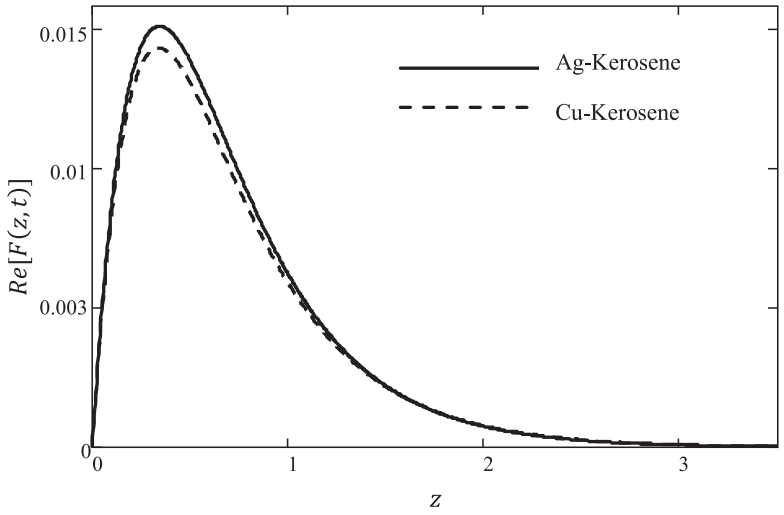

Fig. 5a. Primary velocity of different nanoparticles with kerosene based fluids when $\varphi = 0.2$, $\lambda_1 = \lambda = 1$, $r = 0.5$, $K = 1$, $Ha = 1$, $Gr = 1$, $Pr = 21$, $Rd = 1$ and $t = 1$.

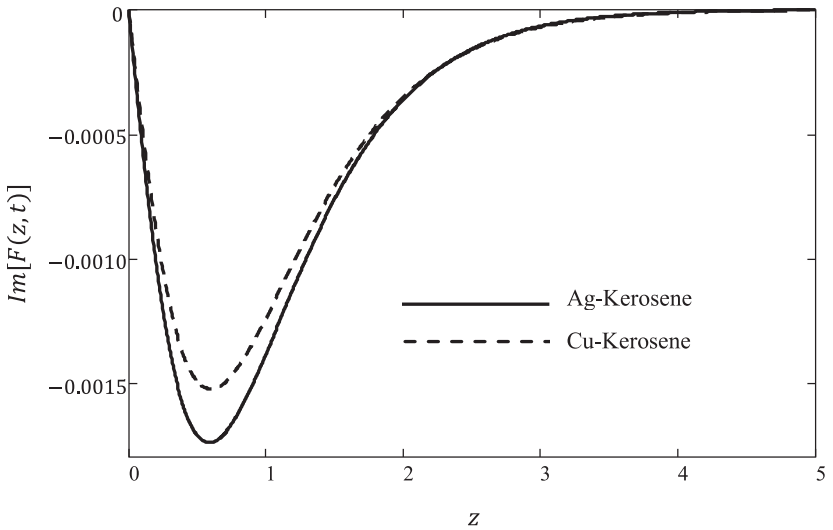

Fig. 5b. Secondary velocity of different nanoparticles with kerosene based fluids when $\varphi = 0.2$, $\lambda_1 = \lambda = 1$, $r = 0.5$, $K = 1$, $Ha = 1$, $Gr = 1$, $Pr = 21$, $Rd = 1$ and $t = 1$.

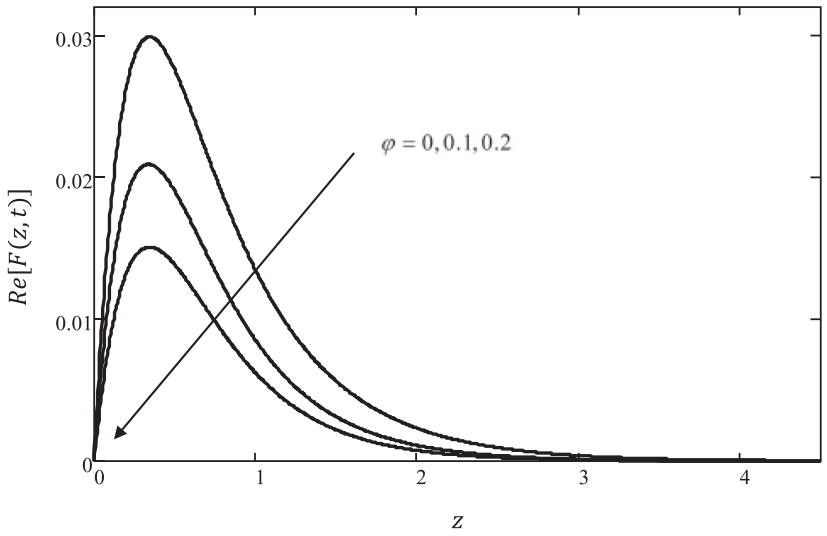

Fig. 6a. Primary velocity for different values of φ of Ag-Kerosene when $\lambda_1 = \lambda = 1$, $r = 0.5$, $K = 1$, $Ha = 1$, $Gr = 1$, $Pr = 21$, $Rd = 1$ and $t = 1$.

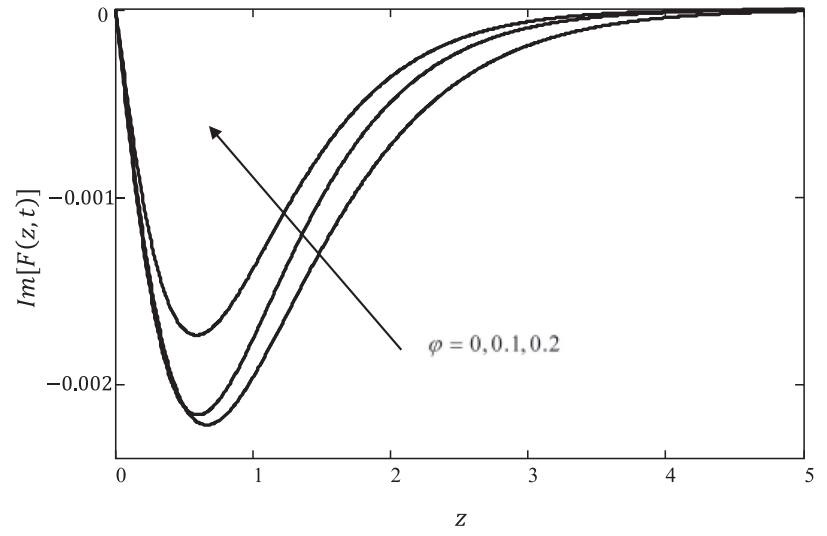

Fig. 6b. Secondary velocity for different values of φ of Ag-Kerosene when $\lambda_1 = \lambda = 1$, $r = 0.5$, $K = 1$, $Ha = 1$, $Gr = 1$, $Pr = 21$, $Rd = 1$ and $t = 1$.

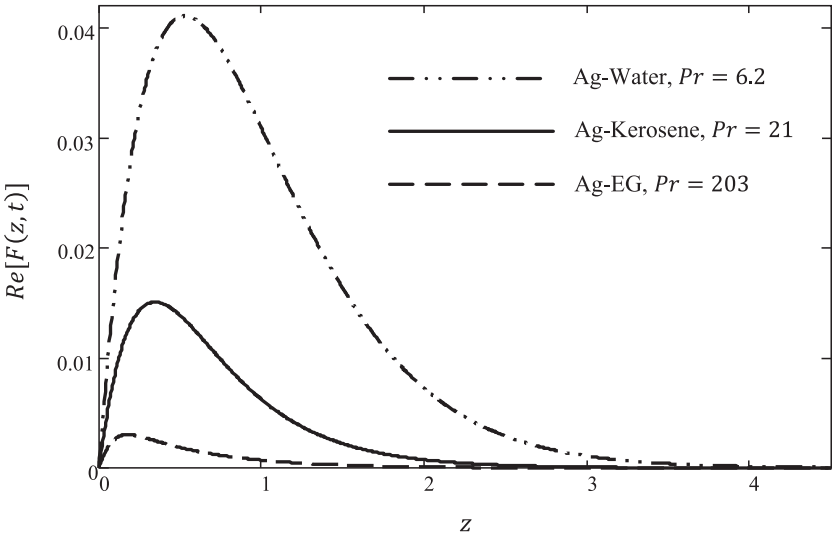

Fig. 7a. Primary velocity of different base fluids for Ag when $\varphi = 0.2$, $\lambda_1 = \lambda = 1$, $r = 0.5$, $K = 1$, $Ha = 1$, $Gr = 1$, $Rd = 1$ and $t = 1$.

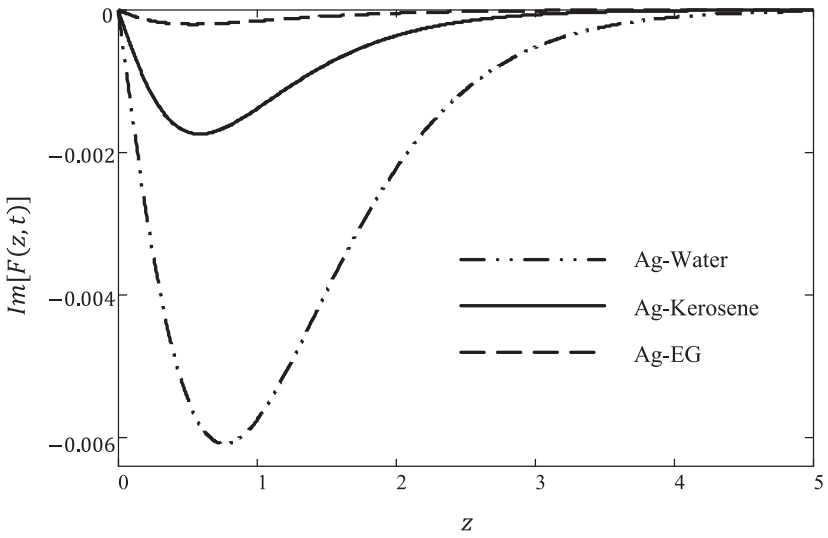

Fig. 7b. Secondary velocity of different base fluids for Ag when $\varphi = 0.2$, $\lambda_1 = \lambda = 1$, $r = 0.5$, $K = 1$, $Ha = 1$, $Gr = 1$, $Rd = 1$ and $t = 1$. .

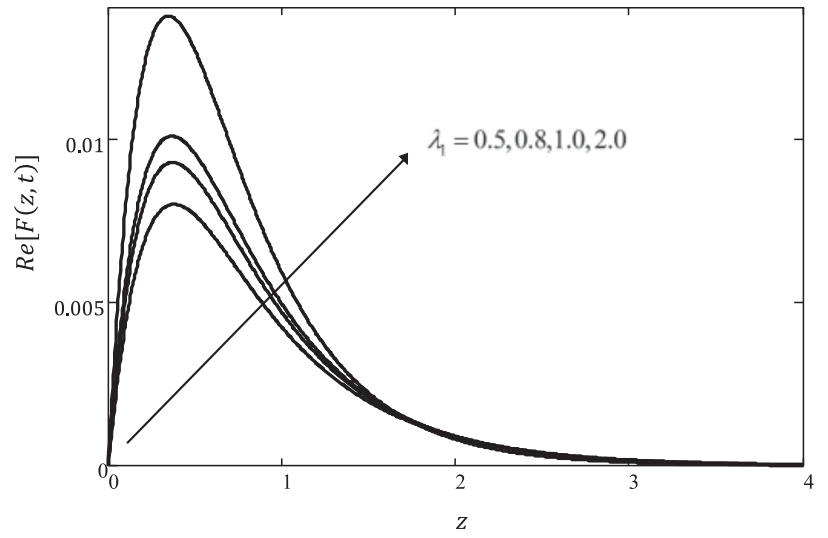

Fig. 8a. Primary velocity of different values of λ_1 of Ag-Kerosene when $\varphi = 0.2$, $\lambda = 2$, $r = 0.5$, $K = 1$, $Ha = 1$, $Gr = 1$, $Pr = 21$, $Rd = 1$ and $t = 1$.

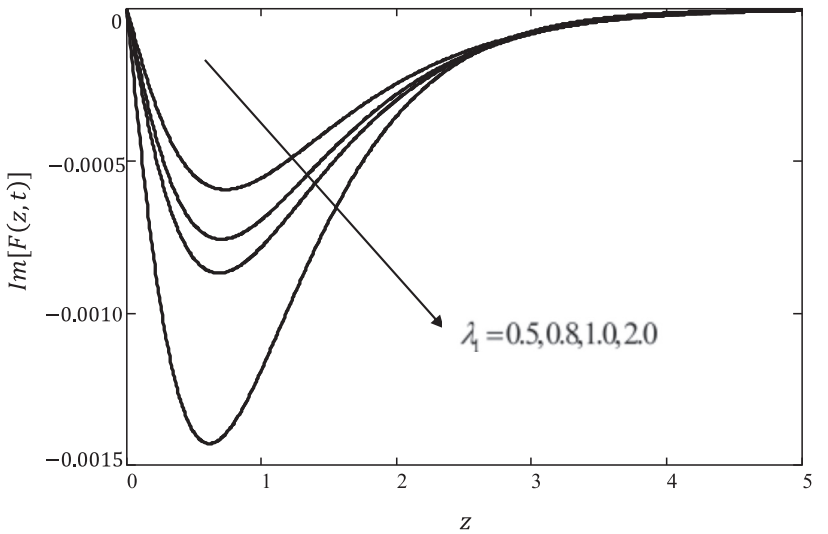

Fig. 8b. Secondary velocity of different values of λ_1 of Ag-Kerosene when $\varphi = 0.2$, $\lambda = 2$, $r = 0.5$, $K = 1$, $Ha = 1$, $Gr = 1$, $Pr = 21$, $Rd = 1$ and $t = 1$.

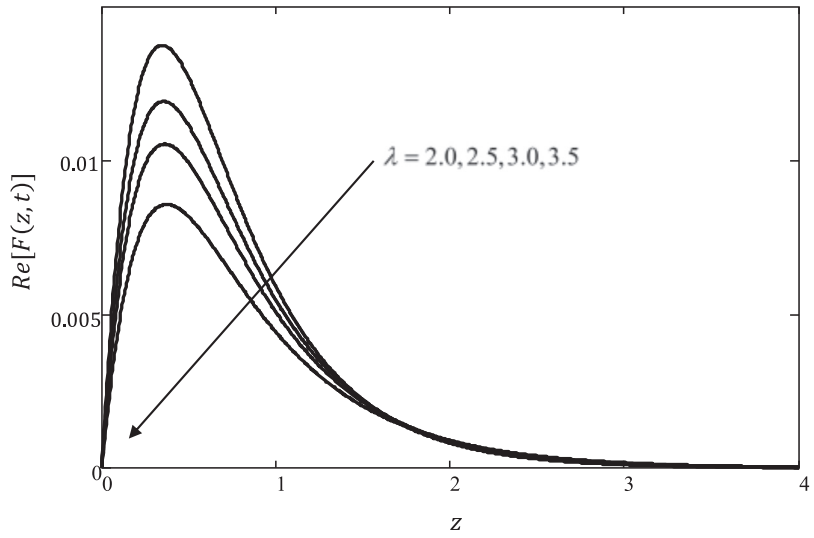

Fig. 9a. Primary velocity of different values of λ of Ag-Kerosene when $\varphi = 0.2$, $\lambda_1 = 2$, $r = 0.5$, $K = 1$, $Ha = 1$, $Gr = 1$, $Pr = 21$, $Rd = 1$ and $t = 1$.

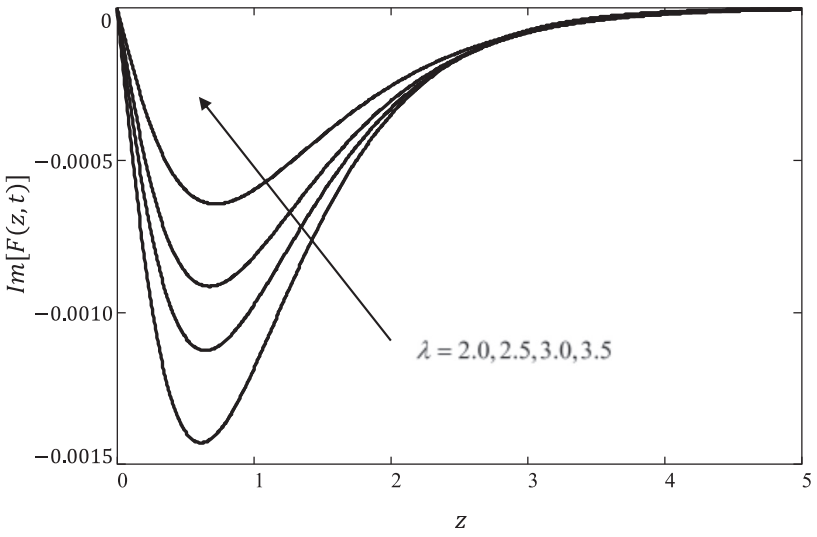

Fig. 9b. Secondary velocity of different values of λ of Ag-Kerosene when $\varphi = 0.2$, $\lambda_1 = 2$, $r = 0.5$, $K = 1$, $Ha = 1$, $Gr = 1$, $Pr = 21$, $Rd = 1$ and $t = 1$.

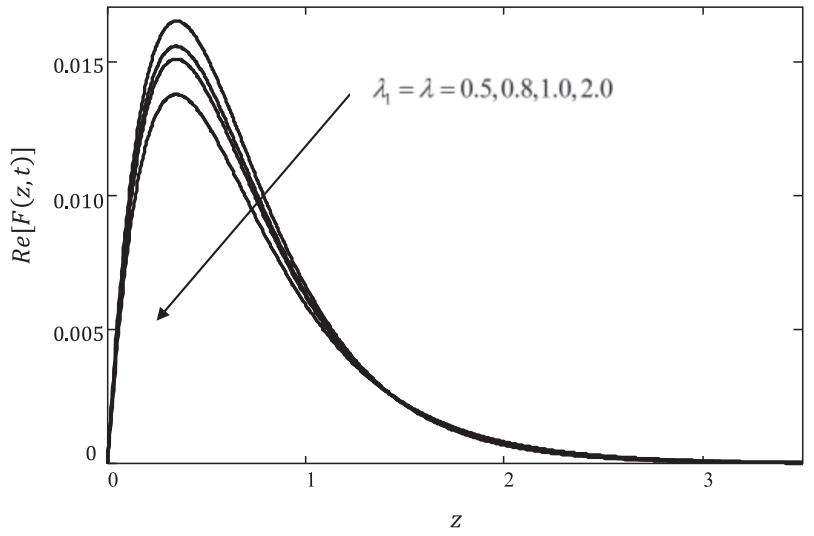

Fig. 10a. Primary velocity of different values of both material parameters of Jeffrey fluid of Ag-Kerosene when $\varphi = 0.2$, $r = 0.5$, $K = 1$, $Ha = 1$, $Gr = 1$, $Pr = 21$, $Rd = 1$ and $t = 1$.

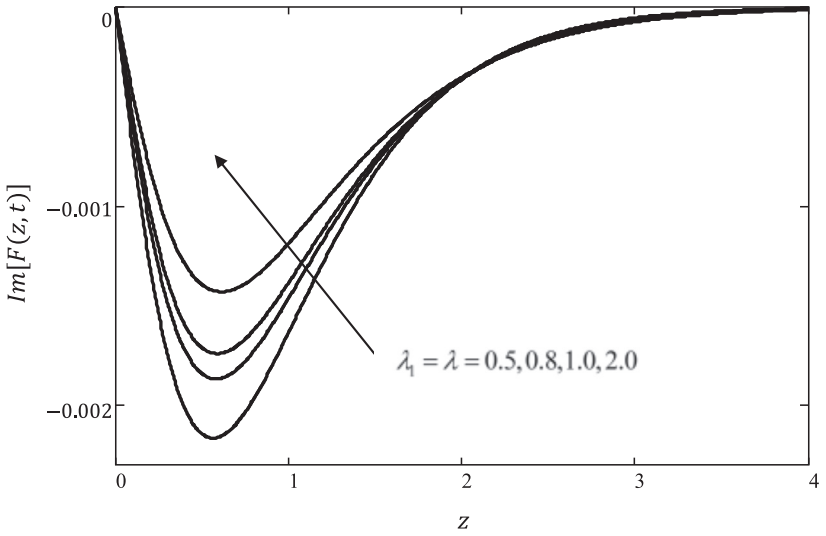

Fig. 10b. Secondary velocity of different values of both material parameters of Jeffrey fluid of Ag-Kerosene when $\varphi = 0.2$, $r = 0.5$, $K = 1$, $Ha = 1$, $Gr = 1$, $Pr = 21$, $Rd = 1$ and $t = 1$.

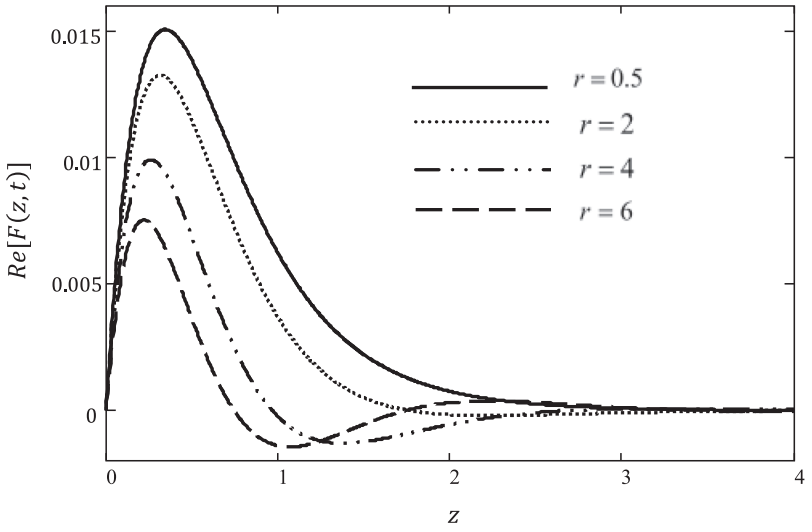

Fig. 11a. Primary velocity of different values of r for Ag-Kerosene when $\varphi = 0.2$, $\lambda_1 = \lambda = 1$, $K = 1$, $Ha = 1$, $Gr = 1$, $Pr = 21$, $Rd = 1$ and $t = 1$.

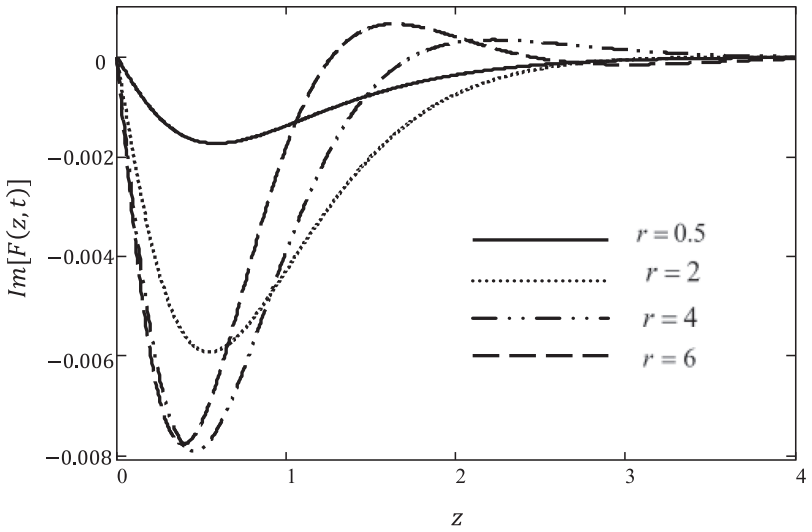

Fig. 11b. Secondary velocity of different values of r for Ag-Kerosene when $\varphi = 0.2$, $\lambda_1 = \lambda = 1$, $K = 1$, $Ha = 1$, $Gr = 1$, $Pr = 21$, $Rd = 1$ and $t = 1$.

rotation no longer accelerates the fluid flow when r is larger. Also, we can say that the Coriolis force acts as a constraint in the fluid flow in the primary flow direction which induces the secondary fluid velocity in the flow field.

The effects of magnetic field or Hartmann number Ha on the velocity components are illustrated in Figs. 12a and 12b respectively. These figures indicate that an increase in the values of Ha tends to reduce the velocity components monotonically due to the Lorentz force, which is similar to the drag force that acts as an agent to retard the fluid flow. Therefore, when we increase the magnetic parameter, the Lorentz force is technically increased and more resistance is given to the motion of the fluid thus decelerating the primary and secondary velocities.

From Figs. 13a and 13b, it is noted that an increase in the permeability parameter of the porous medium K enhances the primary and secondary velocities profiles due to the less friction force, which yields the reverse effect of the magnetic parameter. In fact, higher values of K reduce the resistance of the porous medium, which in turn increase the momentum development of the regime and thus accelerate the fluid flow in primary and secondary velocities.

Moreover, Figs. 14a and 14b reveal that the velocity of components increases when Grashof number Gr increases. In fact, higher values of Gr lead to an increase in the temperature gradient and enhances the buoyancy force. Therefore, it accelerates the primary and secondary fluid velocities throughout the boundary layer region.

Lower values of primary and secondary velocities are seen with the increase of Prandtl number, Pr as presented in Figs. 15a and 15b. Prandtl number is defined as the ratio between momentum diffusivity and thermal diffusivity and hence controls the relative thickness of the momentum and thermal boundary layers. This means that, an increase in the Prandtl number leads to an increase in the viscosity of the fluid which makes the fluid become thick, and consequently decreases the fluid flow.

Figs. 16a and 16b depict that the rise in values of radiation parameter, Rd causes an increase in the flow field. Such a behavior is found because when the intensity of radiation parameter increases, which in turn increases the rate of energy transport to the fluid, the bond holding the components of the fluid particles is easily broken and thus decreases the viscosity. This will make the fluid moves faster which leads to the enhancement of fluid

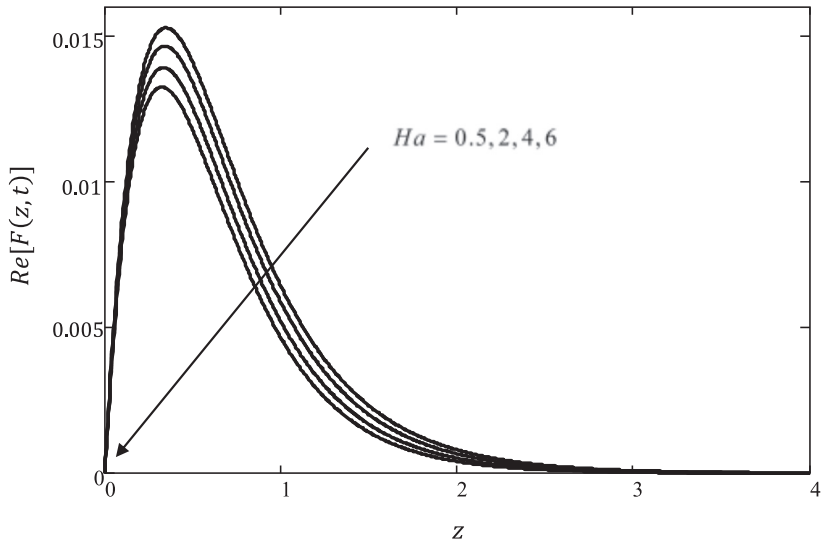

Fig. 12a. Primary velocity of different values of Ha for Ag-Kerosene when $\varphi = 0.2$, $\lambda_1 = \lambda = 1$, $r = 0.5$, $K = 1$, $Gr = 1$, $Pr = 21$, $Rd = 1$ and $t = 1$.

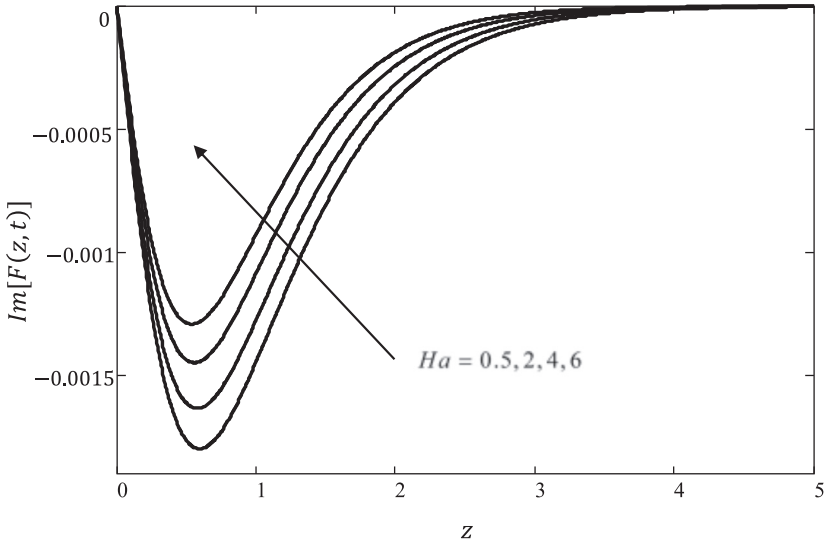

Fig. 12b. Secondary velocity of different values of Ha for Ag-Kerosene when $\varphi = 0.2$, $\lambda_1 = \lambda = 1$, $r = 0.5$, $K = 1$, $Gr = 1$, $Pr = 21$, $Rd = 1$ and $t = 1$.

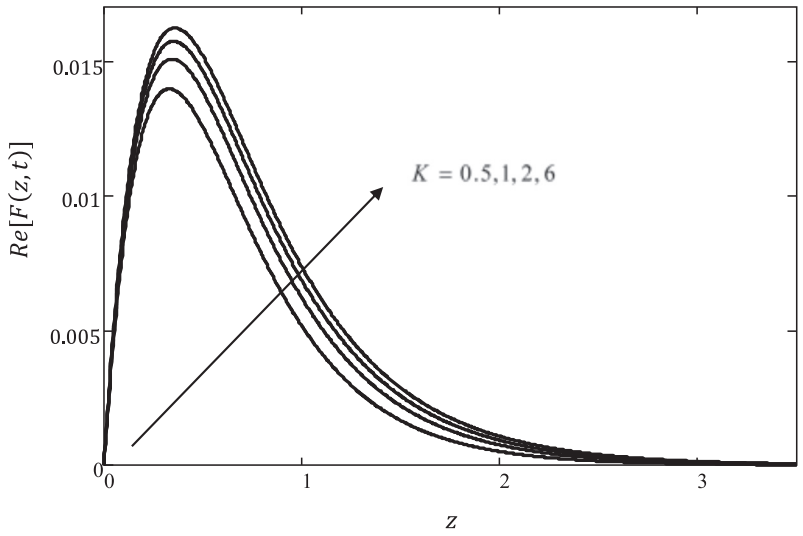

Fig. 13a. Primary velocity of different values of K for Ag-Kerosene when $\varphi = 0.2$, $\lambda_1 = \lambda = 1$, $r = 0.5$, $Ha = 1$, $Gr = 1$, $Pr = 21$, $Rd = 1$ and $t = 1$.

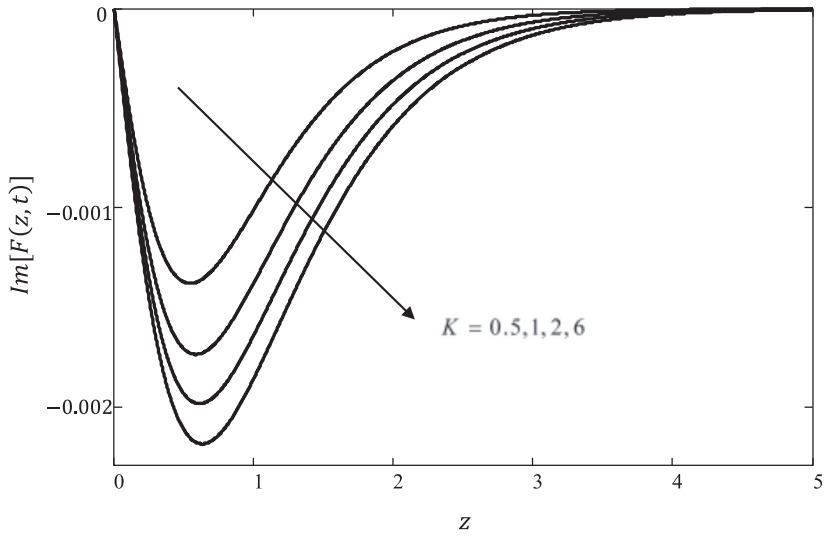

Fig. 13b. Secondary velocity of different values of K for Ag-Kerosene when $\varphi = 0.2$, $\lambda_1 = \lambda = 1$, $r = 0.5$, $Ha = 1$, $Gr = 1$, $Pr = 21$, $Rd = 1$ and $t = 1$.

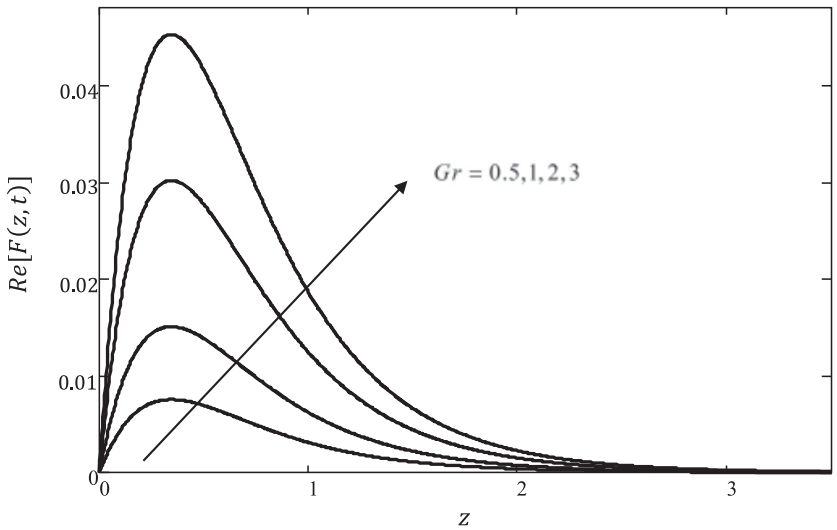

Fig. 14a. Primary velocity of different values of Gr for Ag-Kerosene when $\varphi = 0.2$, $\lambda_1 = \lambda = 1$, $r = 0.5$, $Ha = 1$, $K = 1$, $Pr = 21$, $Rd = 1$ and $t = 1$.

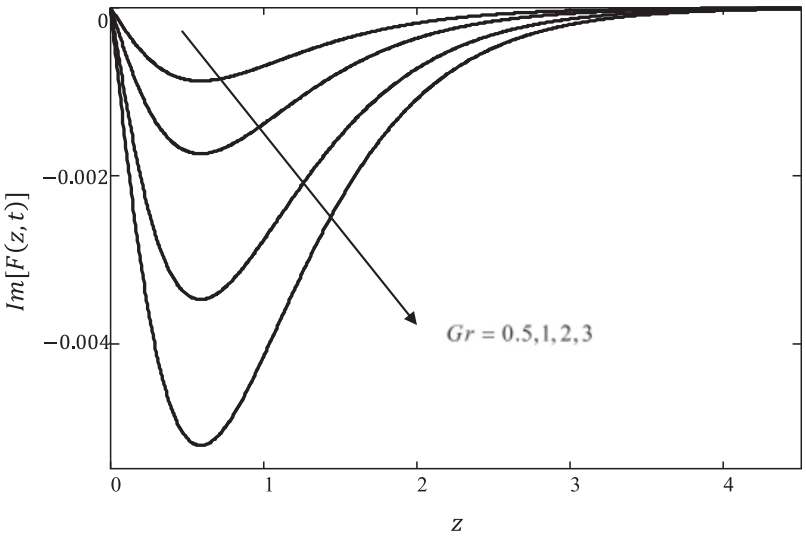

Fig. 14b. Secondary velocity of different values of *Gr* for Ag-Kerosene when $\varphi = 0.2$, $\lambda_1 = \lambda = 1$, $r = 0.5$, $Ha = 1$, $K = 1$, $Pr = 21$, $Rd = 1$ and $t = 1$.

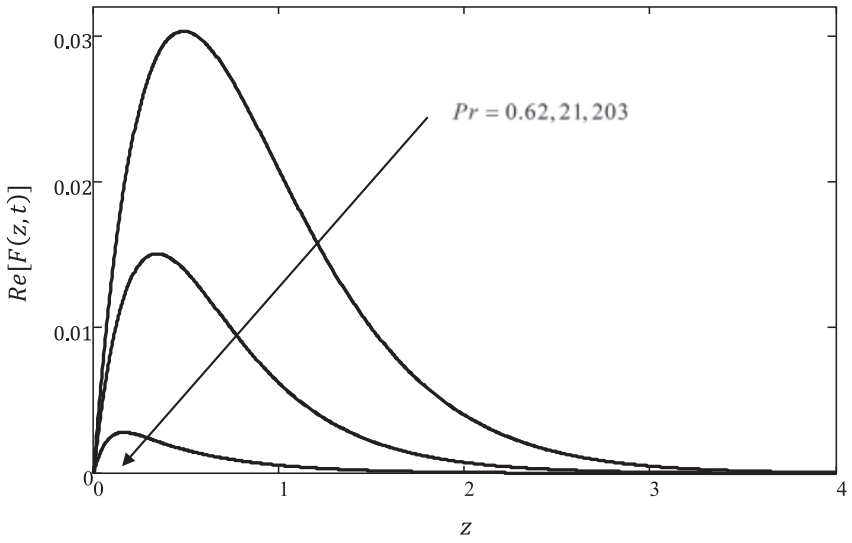

Fig. 15a. Primary velocity of different values of *Pr* for Ag-Kerosene when $\varphi = 0.2$, $\lambda_1 = \lambda = 1$, $r = 0.5$, $Ha = 1$, $K = 1$, $Gr = 1$, $Rd = 1$ and $t = 1$.

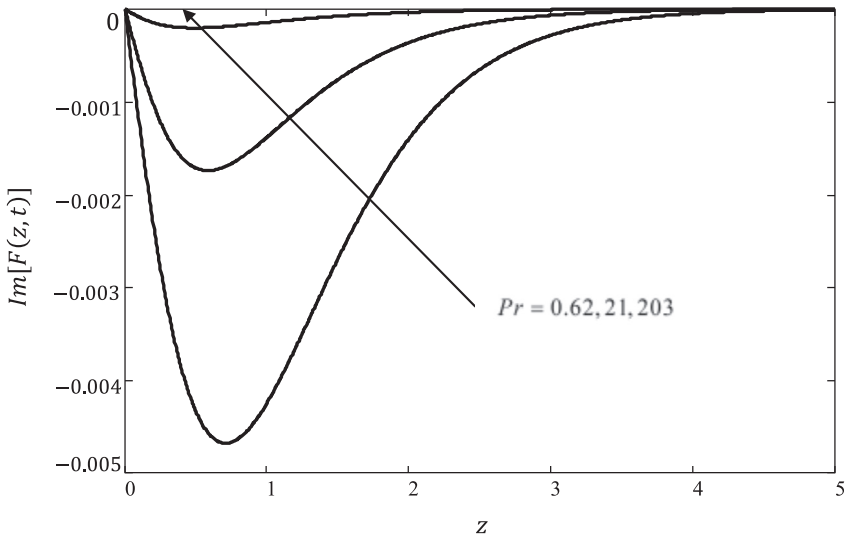

Fig. 15b. Secondary velocity of different values of *Pr* for Ag-Kerosene when $\varphi = 0.2$, $\lambda_1 = \lambda = 1$, $r = 0.5$, $Ha = 1$, $K = 1$, $Gr = 1$, $Rd = 1$ and $t = 1$.

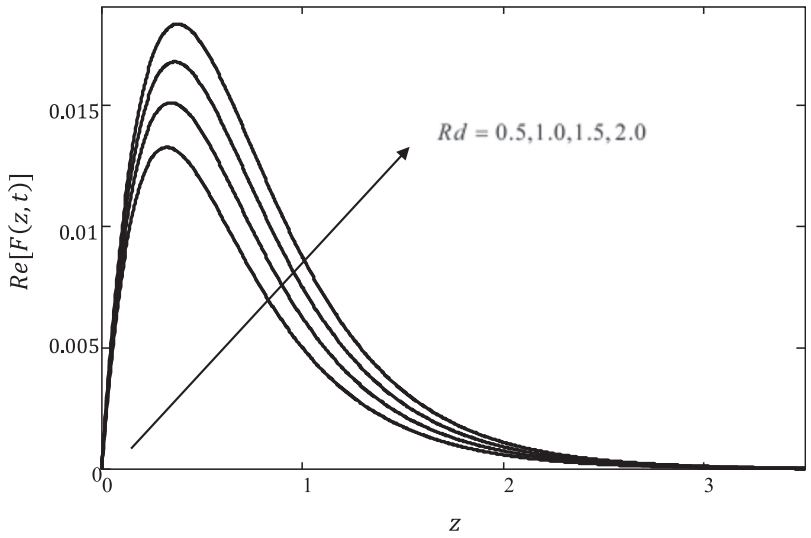

Fig. 16a. Primary velocity of different values of *Rd* for Ag-Kerosene when $\varphi = 0.2$, $\lambda_1 = \lambda = 1$, $r = 0.5$, $Ha = 1$, $K = 1$, $Gr = 1$, $Pr = 21$ and $t = 1$.

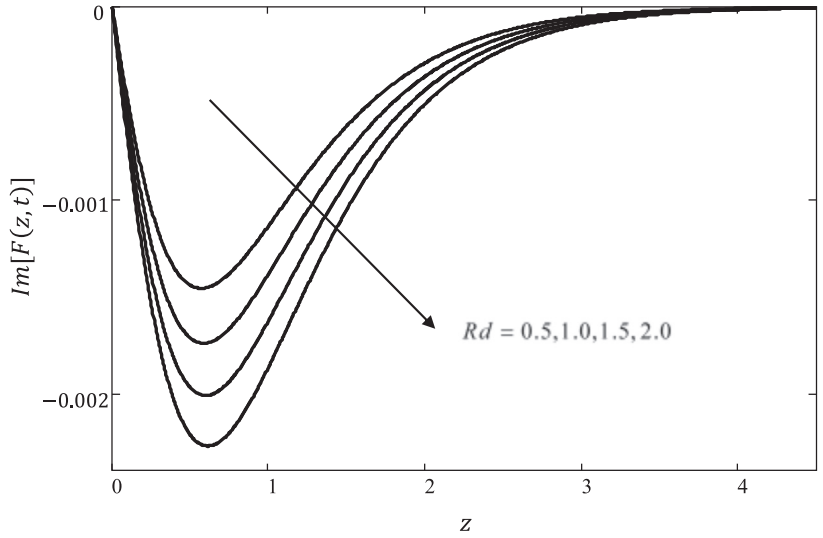

Fig. 16b. Secondary velocity of different values of *Rd* for Ag-Kerosene when $\varphi = 0.2$, $\lambda_1 = \lambda = 1$, $r = 0.5$, $Ha = 1$, $K = 1$, $Gr = 1$, $Pr = 21$ and $t = 1$.

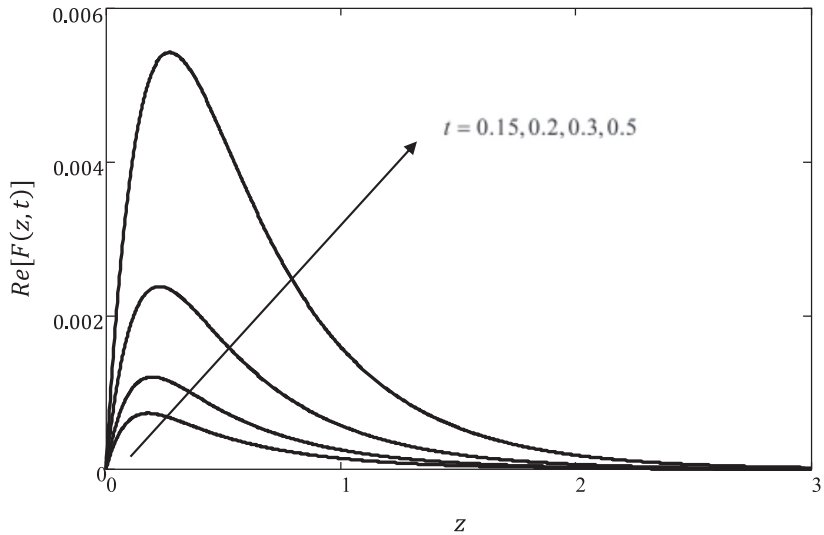

Fig. 17a. Primary velocity of different values of *t* for Ag-Kerosene when $\varphi = 0.2$, $\lambda_1 = \lambda = 1$, $r = 0.5$, $Ha = 1$, $K = 1$, $Gr = 1$, $Pr = 21$ and $Rd = 1$.

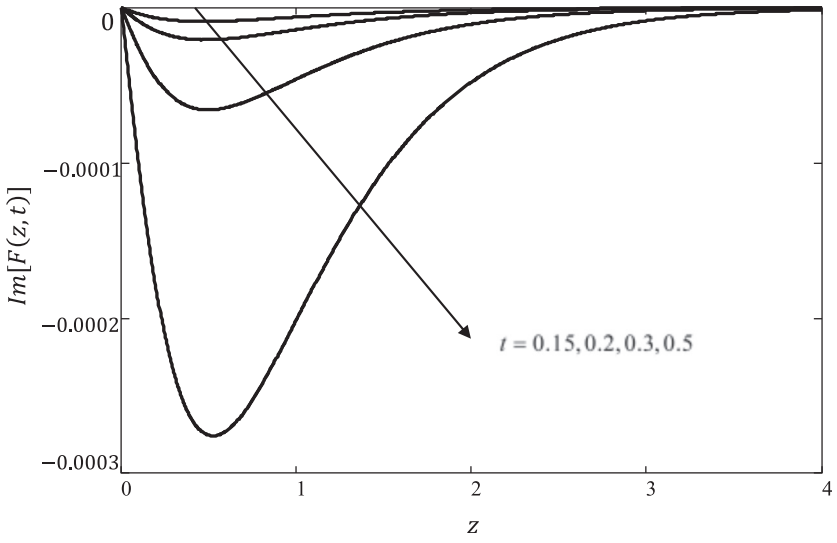

Fig. 17b. Secondary velocity of different values of t for Ag-Kerosene when $\varphi = 0.2$, $\lambda_1 = \lambda = 1$, $r = 0.5$, $Ha = 1$, $K = 1$, $Gr = 1$, $Pr = 21$ and $Rd = 1$.

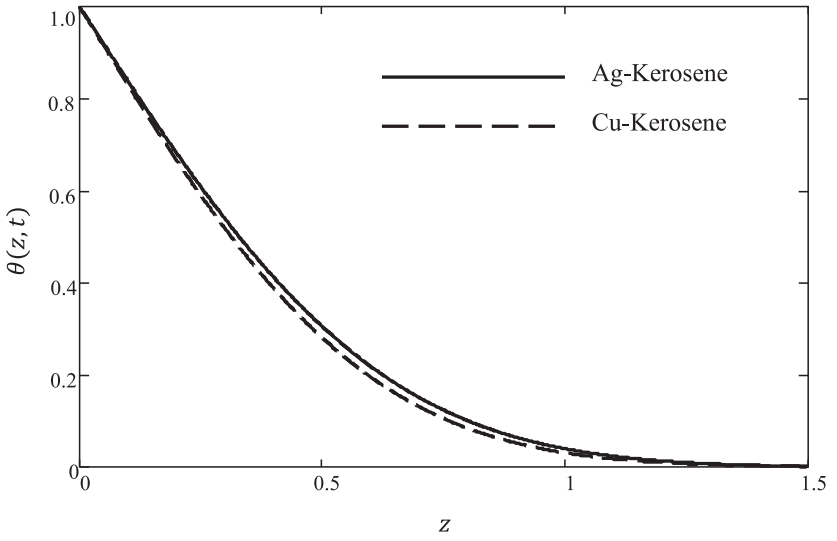

Fig. 18. Temperature profile for different nanoparticles with kerosene as a base fluid when $\varphi = 0.2$, $Rd = 1$, $Pr = 21$ and $t = 1$.

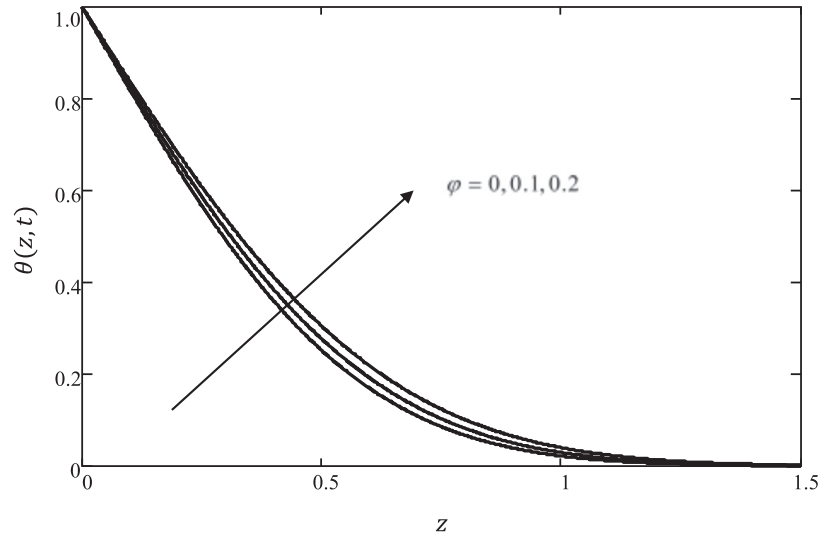

Fig. 19. Temperature profile of different φ of Ag-Kerosene when $Rd = 1$, $Pr = 21$ and $t = 1$.

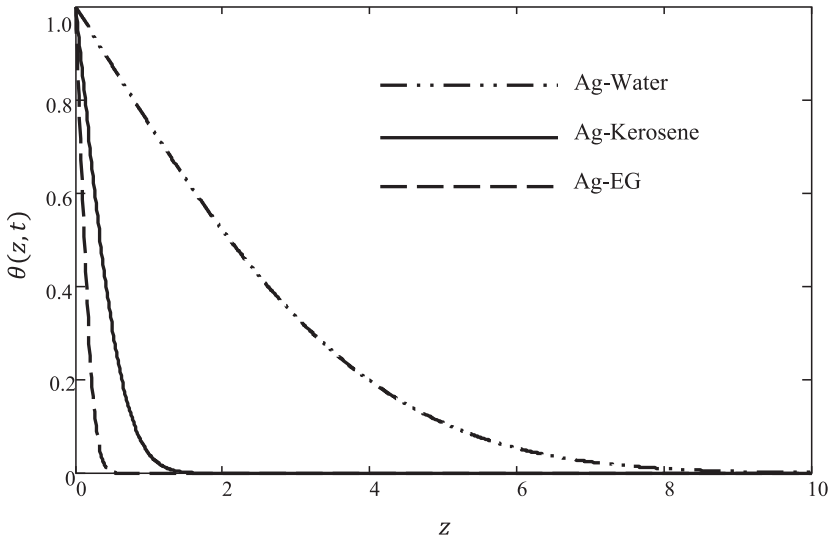

Fig. 20. Temperature profile for different Ag-based fluids (water, kerosene and EG) when $\varphi = 0.2$, $Rd = 1$ and $t = 1$.

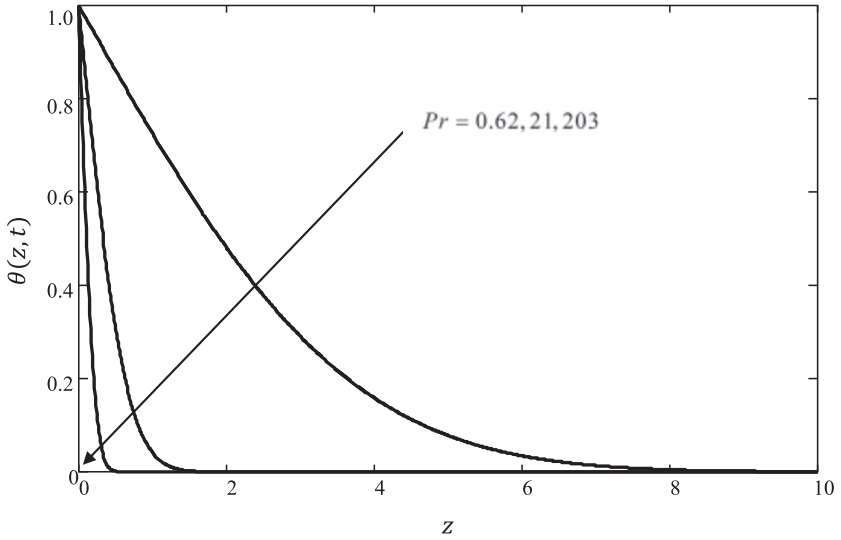

Fig. 21. Temperature profile of Ag-Kerosene for different values of Pr when $\varphi = 0.2$, $Rd = 1$ and $t = 1$.

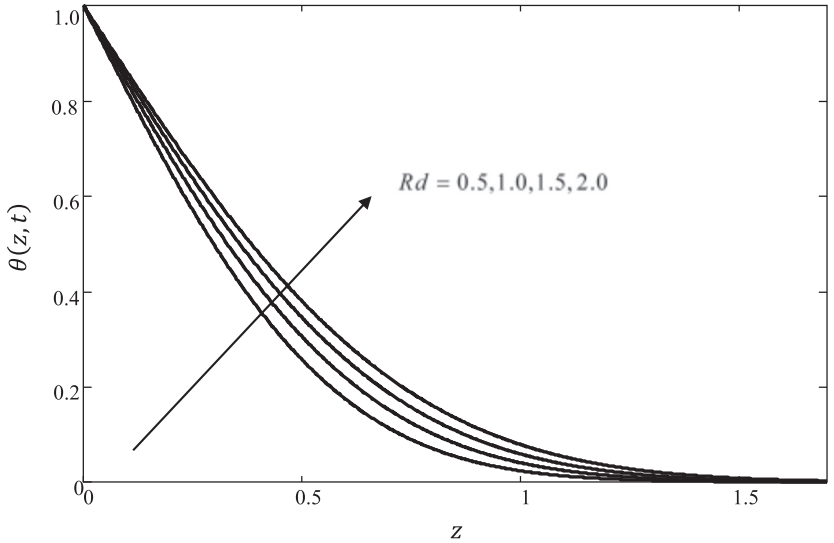

Fig. 22. Temperature profile for different values of Rd when $\varphi = 0.2$, $Pr = 21$ and $t = 1$.

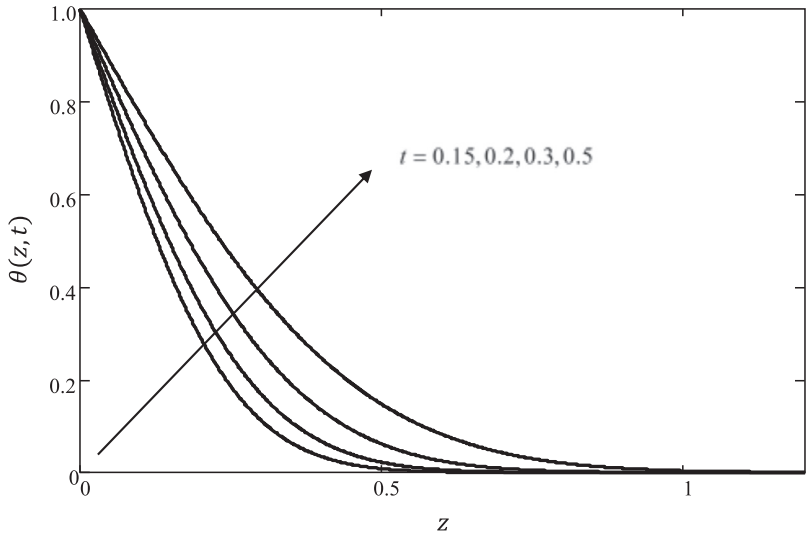

Fig. 23. Temperature profile of Ag-Kerosene for different values of t when $\varphi = 0.2$, $Pr = 21$ and $t = 1$.

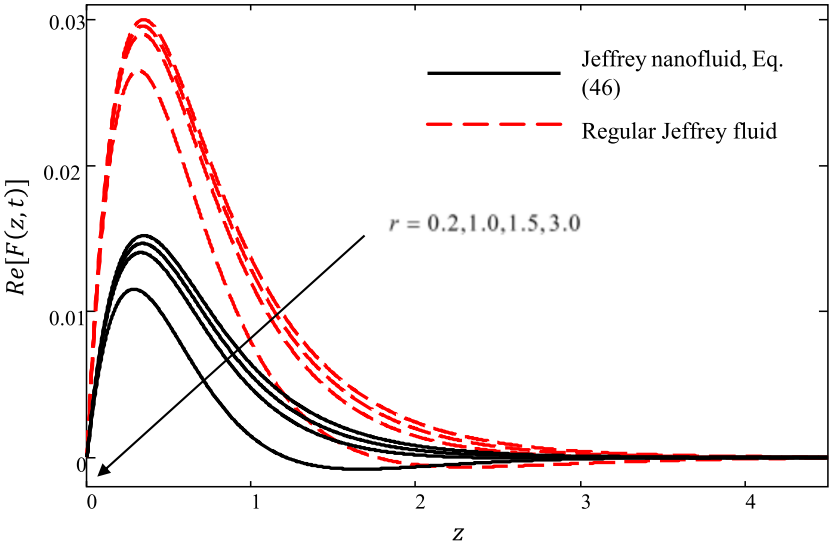

Fig. 24a. Comparison of primary velocity profile between Jeffrey nanofluid and regular Jeffrey fluid for different values of r for Ag-Kerosene when $\lambda_1 = \lambda = 1$, $K = 1$, $Ha = 1$, $Gr = 1$, $Pr = 21$, $Rd = 1$ and $t = 1$.

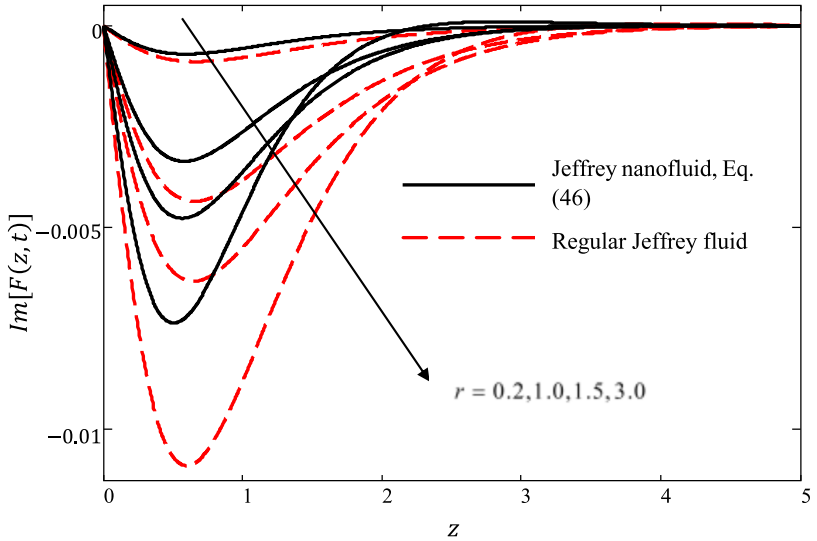

Fig. 24b. Comparison of Secondary velocity profile between Jeffrey nanofluid and regular Jeffrey fluid for different values of r for Ag-Kerosene when $\lambda_1 = \lambda = 1$, $K = 1$, $Ha = 1$, $Gr = 1$, $Pr = 21$, $Rd = 1$ and $t = 1$.

velocity for primary and secondary flow directions. Also, Figs. 17a and 17b show that the velocity profiles increase with the increase of time, t.

The variation of AgNPs and CuNPs on temperature profile is illustrated in Fig. 18. It is found that AgNPs have higher temperature compared to the CuNPs as we have noticed in velocity components. It shows that AgNPs have smallest thermal boundary layer thickness and different nanoparticles make changes in velocity and temperature profiles.

Fig. 19 is presented to show the effect of nanoparticles' volume fraction on temperature profile. It is clear from this figure that enhancement in volume fraction of nanoparticles leads to the rise of temperature distributions. This is due to the fact that an increase in the nanoparticles' volume fraction leads to the increase in the thermal conductivity and this enhances the thermal boundary layer thickness, which causes the temperature to increase. Fig. 20 sketches a comparison of different types of base fluid on temperature and it is found that Ag-water based produces higher temperature compared to other mixtures.

Besides that, Fig. 21 exhibits the characteristics of the Prandtl number Pr on temperature distribution. It is noticed that a higher Prandtl number leads to a fall in temperature profiles due to the fact that lower Pr values have more uniform temperature distribution across the thermal boundary layer as compared to higher Pr. In this case, lower values of Pr, fluids possess high thermal conductivity which causes the heat to diffuse away from the heated surface more rapidly and faster compare to higher values of Pr. Thus, it increases the boundary layer thickness and consequently decreases the temperature distribution.

On the other hand, the effect of radiation parameter Rd on temperature is analyzed in Fig. 22. The temperature profile rapidly increases as the radiation parameter increases. A similar behavior is also expected since the radiation parameter signifies the relative contribution of conduction heat transfer to thermal radiation transfer. We can say that the thermal radiation provides an additional means to diffuse energy. Finally, Fig. 23 reveals that the fluid temperature increases upon increasing the dimensionless time, t.

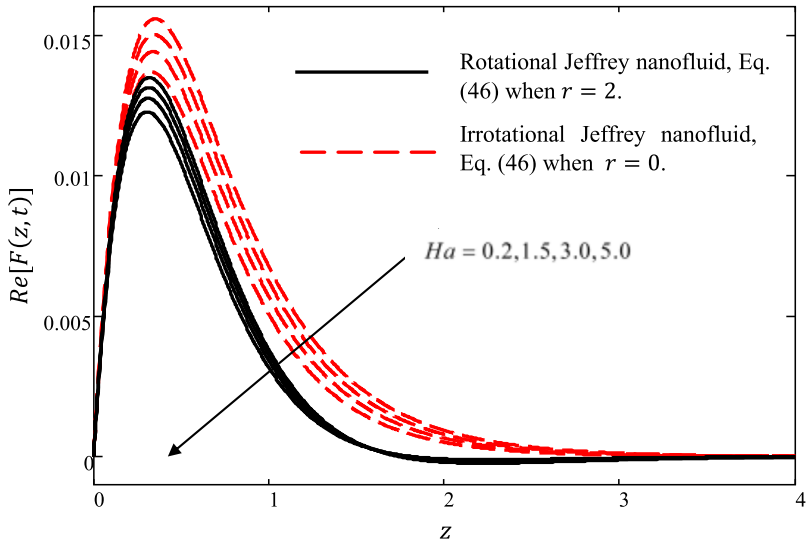

Fig. 25a. Comparison of primary velocity profile between rotational and irrotational Jeffrey nanofluids (Ag-Kerosene) for different values of Ha when $\lambda_1 = \lambda = 1$, $K = 1$, $Gr = 1$, $Pr = 21$, $Rd = 1$ and $t = 1$.

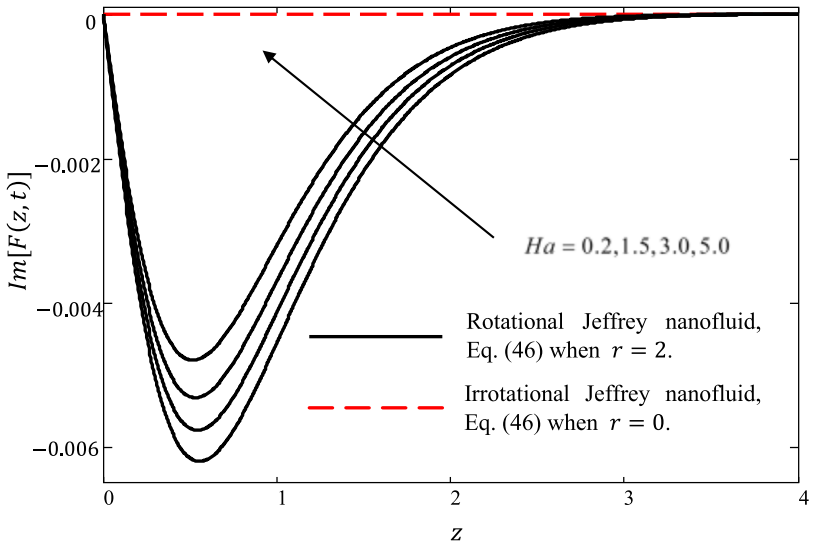

Fig. 25b. Comparison of secondary velocity profile between rotational and irrotational Jeffrey nanofluids (Ag-Kerosene) for different values of Ha when $\lambda_1 = \lambda = 1$, $K = 1$, $Gr = 1$, $Pr = 21$, $Rd = 1$ and $t = 1$.

Table 2
Variation of skin friction of Ag-Kerosene for different values of parameters.

t	φ	$\lambda_1 = \lambda$	r	Ha	K	Gr	Pr	Rd	Re $[\tau(t)]$	$-$Im $[\tau(t)]$
0.1	0	0.5	0.5	0.5	0.5	0.5	6.2	0.5	**0.064**	**0.0002568**
0.2	0	0.5	0.5	0.5	0.5	0.5	6.2	0.5	**0.080**	**0.0008317**
0.3	0	0.5	0.5	0.5	0.5	0.5	6.2	0.5	**0.089**	**0.001580**
0.4	**0**	0.5	0.5	0.5	0.5	0.5	6.2	0.5	**0.095**	**0.002425**
0.4	**0.1**	0.5	0.5	0.5	0.5	0.5	6.2	0.5	**0.097**	**0.002651**
0.4	**0.2**	0.5	0.5	0.5	0.5	0.5	6.2	0.5	**0.098**	**0.002892**
0.4	0.2	**1.0**	0.5	0.5	0.5	0.5	6.2	0.5	**0.086**	**0.002330**
0.4	0.2	**1.5**	0.5	0.5	0.5	0.5	6.2	0.5	**0.082**	**0.002094**
0.4	0.2	**2.0**	0.5	0.5	0.5	0.5	6.2	0.5	**0.079**	**0.001963**
0.4	0.2	2.0	**1.0**	0.5	0.5	0.5	6.2	0.5	**0.079**	**0.003919**
0.4	0.2	2.0	**1.5**	0.5	0.5	0.5	6.2	0.5	**0.079**	**0.005861**
0.4	0.2	2.0	**2.0**	0.5	0.5	0.5	6.2	0.5	**0.078**	**0.007782**
0.4	0.2	2.0	2.0	**1.0**	0.5	0.5	6.2	0.5	**0.077**	**0.007592**
0.4	0.2	2.0	2.0	**1.5**	0.5	0.5	6.2	0.5	**0.076**	**0.007409**
0.4	0.2	2.0	2.0	**2.0**	0.5	0.5	6.2	0.5	**0.075**	**0.007232**
0.4	0.2	2.0	2.0	2.0	**1.0**	0.5	6.2	0.5	**0.086**	**0.009457**
0.4	0.2	2.0	2.0	2.0	**1.5**	0.5	6.2	0.5	**0.090**	**0.010000**
0.4	0.2	2.0	2.0	2.0	**2.0**	0.5	6.2	0.5	**0.092**	**0.011000**
0.4	0.2	2.0	2.0	2.0	2.0	**1.0**	6.2	0.5	**0.184**	**0.022000**
0.4	0.2	2.0	2.0	2.0	2.0	**1.5**	6.2	0.5	**0.276**	**0.033000**
0.4	0.2	2.0	2.0	2.0	2.0	**2.0**	6.2	0.5	**0.368**	**0.044000**
0.4	0.2	2.0	2.0	2.0	2.0	2.0	**21**	0.5	**0.267**	**0.018000**
0.4	0.2	2.0	2.0	2.0	2.0	2.0	**203**	0.5	**0.106**	**0.002355**
0.4	0.2	2.0	2.0	2.0	2.0	2.0	203	**1.0**	**0.116**	**0.002842**
0.4	0.2	2.0	2.0	2.0	2.0	2.0	203	**1.5**	**0.125**	**0.003321**
0.4	0.2	2.0	2.0	2.0	2.0	2.0	203	**2.0**	**0.133**	**0.003792**

Table 3
Variation of Nusselt number of Ag-Kerosene based Jeffrey nanofluid for different values of parameters.

t	φ	Pr	Rd	Nu
0.1	0	6.2	0.5	**3.627**
0.2	0	6.2	0.5	**2.565**
0.3	0	6.2	0.5	**2.094**
0.4	**0**	6.2	0.5	**1.814**
0.4	**0.1**	6.2	0.5	**1.682**
0.4	**0.2**	6.2	0.5	**1.555**
0.4	0.2	**21**	0.5	**2.862**
0.4	0.2	**203**	0.5	**8.900**
0.4	0.2	203	**1.0**	**8.050**
0.4	0.2	203	**1.5**	**7.405**
0.4	0.2	203	**2.0**	**6.893**

For the sake of comparison, we have plotted the present result (46) with the regular Jeffrey fluid for different values of r as shown in Figs. 24a and 24b. It is found that the amplitude of regular Jeffrey fluid is higher compared to the Jeffrey nanofluid. This means that the Jeffrey nanofluid has higher viscosity than regular Jeffrey fluid, and this high viscosity decreases the fluid flow. Meanwhile, Figs. 25a and 25b give a comparison for rotational and irrotational effects on velocity profiles for different values of Ha. Obviously, rotation effect reduces the velocity profiles compared to fluids without the rotation effect. This is also may be due to the presence of Coriolis force.

The numerical results for skin friction and Nusselt number are computed from the analytical expressions (48) and (49) presented in Table 2 and Table 3 for various parameters of interest. It is observed that the primary skin friction decreases upon increasing λ, r, Ha and Pr whereas it increases upon increasing φ, K, Gr, Rd and t. Meanwhile, for secondary skin friction, it increases upon increasing φ, r, K, Gr, Rd and t, whereas decreases upon increasing λ, Ha and Pr. On the other hand, from Table 3, it is depicted that the rate of heat transfer decreases for large values of t, φ and Rd. However, this behavior is quite opposite for Pr.

Conclusion

The unsteady MHD free convection flow of rotating Jeffrey nanofluid that is saturated in a porous medium under the influence of thermal radiation using Tiwari and Das nanofluid model is investigated analytically using the Laplace transform technique. The fluid is filled with AgNPs and Kerosene oil is used as the base fluid. A comparative study between the present results and the previous published work is presented to authenticate our results and an excellent agreement is found. The following main points can be drawn from this study:

- AgNPs have higher velocity and thermal heat transfer compared to CuNPs.
- EG-base fluid are concluded to have lower velocity than Kerosene oil and water. This shows a greater viscosity and thermal conductivity of EG-base fluid.
- An increase in r tends to retard the primary fluid flow but enhances the secondary fluid flow.
- It is also recorded that the Coriolis force has the tendency to decrease the velocity of the fluid when we make a comparison between solutions with rotational and irrotational effects.

- Increasing the *Ha* leads to the enhancement of the Lorentz force which acts as a resistance to the fluid motion. As a result, it decreases the velocity.
- Also, a rise in *Gr* increases the temperature gradient which enhances the buoyancy force and consequently increases the velocity profile.
- The velocity profile decreases with an increasing volume fraction of nanoparticle, while the increase in temperature profile significantly increases the rate of heat transfer.
- Increase in *Pr* leads to the decrease in both velocity and temperature profiles.
- Increasing values of *K* and *Rd* give rise in the fluid flow.
- Interestingly, the present result (46) can be reduced to rotating second grade nanofluid when λ_1 is neglected.

Acknowledgments

The authors would like to acknowledge the Ministry of Higher Education (MOHE) and Research Management Centre-UTM for the financial support through vote numbers 4F713, 4F538 and 06H67 for this research. The last author wants to acknowledge with thanks the Deanship of Scientific Research (DSR) at King Abdulaziz University, Jeddah for technical and financial support.

References

[1] Choi SUS, Eastman JA. Enhancing thermal conductivity of fluids with nanoparticles. In: Developments and applications of non-Newtonian flows. p. 99–105.
[2] Mohyud-Din S, Khan U, Ahmed N, Hassan S. Magnetohydrodynamic flow and heat transfer of nanofluids in stretchable convergent/divergent channels. Appl Sci 2015;5:1639–64.
[3] Mohyud-Din ST, Khan U, Ahmed N, Bin-Mohsin B. Heat and mass transfer analysis for mhd flow of nanofluid inconvergent/divergent channels with stretchable walls using buongiorno's model. In: Neural Comput Appl. p. 1–14.
[4] Haq RU, Nadeem S, Khan ZH, Noor NFM. MHD squeezed flow of water functionalized metallic nanoparticles over a sensor surface. Phys E Low-dimensional Syst Nanostruct 2015;73:45–53.
[5] Haq RU, Khan ZH, Hussain ST, Hammouch Z. Flow and heat transfer analysis of water and ethylene glycol based Cu nanoparticles between two parallel disks with suction/injection effects. J Mol Liq 2016;221:298–304.
[6] Haq RU, Noor NFM, Khan ZH. Numerical simulation of water based magnetite nanoparticles between two parallel disks. Adv Powder Technol 2016:1–8.
[7] Dinarvand S, Abbassi A, Hosseini R, Pop I. Homotopy analysis method for mixed convective boundary layer flow of a nanofluid over a vertical circular cylinder. Therm Sci 2015;19(2):549–61.
[8] Dinarvand S, Hosseini R, Pop I. Homotopy analysis method for unsteady mixed convective stagnation-point flow of a nanofluid using Tiwari-das nanofluid model. Int J Numer Methods Heat Fluid Flow 2016;26(1):40–62.
[9] Dinarvand S, Hosseini R, Abulhasansari M, Pop I. Buongiorno's model for double-diffusive mixed convective stagnation-point flow of a nanofluid considering diffusiophoresis effect of binary base fluid. Adv Powder Technol 2015;26(5):1423–34.
[10] Dinarvand S, Hosseini R, Pop I. Unsteady convective heat and mass transfer of a nanofluid in howarth's stagnation point by Buongiorno's model. Int J Numer Methods Heat Fluid Flow 2015;25(5):1176–97.
[11] Khan U, Ahmed N, Mohyud-Din ST. Heat transfer effects on carbon nanotubes suspended nanofluid flow in a channel with non-parallel walls under the effect of velocity slip boundary condition: a numerical study. Neural Comput Appl 2015.
[12] Khan U, Mohyud-Din ST, Bin-Mohsin B. Convective heat transfer and thermo-diffusion effects on flow of nanofluid towards a permeable stretching sheet saturated by a porous medium. Aerosp Sci Technol 2016;50:196–203.
[13] Khan U, Ahmed N, Tauseef S. Analysis of magnetohydrodynamic flow and heat transfer of Cu – water nanofluid between parallel plates for different shapes of nanoparticles. Neural Comput Appl 2016:1–9.
[14] Khan U, Ahmed N, Mohyud-Din ST. Influence of viscous dissipation and joule heating on MHD bio-convection flow over a porous wedge in the presence of nanoparticles and gyrotactic microorganisms. Springerplus 2016;5 (2043):1–18.
[15] Khan WA, Khan ZH, Haq RU. Flow and heat transfer of ferrofluids over a flat plate with uniform heat flux. Eur Phys J Plus 2015;130(86).
[16] Haq RU, Khan ZH, Khan WA. Thermophysical effects of carbon nanotubes on MHD flow over a stretching surface. Phys E 2014;63:215–22.
[17] Haq RU, Nadeem S, Khan ZH, Noor NFM. Convective heat transfer in MHD slip flow over a stretching surface in the presence of carbon nanotubes. Phys B Phys Condens Matter 2015;457:40–7.
[18] Haq RU, Rajotia D, Noor NFM. Thermophysical effects of water driven copper nanoparticles on MHD axisymmetric permeable shrinking sheet: dual-nature study. Eur Phys J Plus 2016;39(33):1–12.
[19] Shahzad F, Haq RU, Al-mdallal QM. Water driven Cu nanoparticles between two concentric ducts with oscillatory pressure gradient. J Mol Liq 2016;224:322–32.
[20] Haq R, Shahzad F, Al-mdallal QM. MHD pulsatile flow of engine oil based carbon nanotubes between two concentric cylinders. Results Phys. 2017;7:57–68.
[21] Saleem S, Nadeem S, Haq RU. Buoyancy and metallic particle effects on an unsteady water-based fluid flow along a vertically rotating cone. Eur Phys J Plus 2014;129(213):1–8.
[22] Hosseini M, Mohammadian E, Shirvani M, Mirzababaei SN, Shakeri Aski F. Thermal analysis of rotating system with porous plate using nanofluid. Powder Technol 2014;254:563–71.
[23] Sheikholeslami M, Hatami M, Ganji DD. Nanofluid flow and heat transfer in a rotating system in the presence of a magnetic field. J Mol Liq 2014;190:112–20.
[24] Hussain ST, Haq R, Khan ZH, Nadeem S. Water driven flow of carbon nanotubes in a rotating channel. J Mol Liq 2016;214:136–44.
[25] Tiwari RK, Das MK. Heat transfer augmentation in a two-sided lid-driven differentially heated square cavity utilizing nanofluids. Int J Heat Mass Transf 2007;50:2002–18.
[26] Sheikholeslami M, Ganji DD. Three dimensional heat and mass transfer in a rotating system using nanofluid. Powder Technol 2014;253:789–96.
[27] Buongiorno J. Convective transport in nanofluids. J Heat Transfer 2006;128:240–50.
[28] Khan U, Ahmed N, Mohyud-din ST. Numerical investigation for three dimensional squeezing flow of nanofluid in a rotating channel with lower stretching wall suspended by carbon nanotubes. Appl Therm Eng 2017;113:1107–17.
[29] Nadeem S, Rehman AU, Mehmood R. Boundary layer flow of rotating two phase nanofluid over a stretching surface. Heat Transf Res 2016;45(3):285–98.
[30] Sree K, Ranga Vani DR, Prasada Rao DRV. Effect of thermal radiation on unsteady convective heat transfer flow of a rotating nano-fluid past a vertical plate. Adv. Appl. Sci. Res. 2016;7(3):83–94.
[31] Das K. Flow and heat transfer characteristics of nanofluids in a rotating frame. Alexandria Eng J 2014;53:757–66.
[32] Raza J, Mohd Rohni A, Omar Z, Awais M. Heat and mass transfer analysis of MHD nanofluid flow in a rotating channel with slip effects. J Mol Liq 2016;219:703–8.
[33] Mohyud-Din ST, Zaidi ZA, Khan U, Ahmed N. On heat and mass transfer analysis for the flow of a nanofluid between rotating parallel plates. Aerosp Sci Technol 2015;46:514–22.
[34] Satya Narayana PV, Venkateswarlu B, Venkataramana S. Thermal radiation and heat source effects on a MHD nanofluid past a vertical plate in a rotating system with porous medium. Heat Transf Res 2015;44(1):1–19.
[35] Hayat T, Qayyum S, Imtiaz M, Alsaedi A. Three-dimensional rotating flow of jeffrey fluid for cattaneo-christov heat flux model. AIP Adv 2016;6:1–11.
[36] Hussain T, Shehzad SA, Hayat T, Alsaedi A, Al-solamy F, Ramzan M. Radiative hydromagnetic flow of jeffrey nanofluid by an exponentially stretching sheet. PLoS ONE 2014;9(8):1–9.
[37] Hayat T, Muhammad T, Shehzad SA, Alsaedi A. Three-dimensional flow of jeffrey nanofluid with a new mass flux condition. J Aerosp Eng 2016;29 (2):1–8.
[38] Shehzad SA, Hayat T, Alsaedi A, Obid MA. Nonlinear thermal radiation in three-dimensional flow of Jeffrey nanofluid: a model for solar energy. Appl Math Comput 2014;248:273–86.
[39] Shehzad SA, Abdullah Z, Alsaedi A, Abbasi FM, Hayat T. Thermally radiative three-dimensional flow of jeffrey nanofluid with internal heat generation and magnetic field. J Magn Magn Mater 2016;397:108–14.
[40] Hayat T, Imtiaz M, Alsaedi A. Magnetohydrodynamic stagnation point flow of a Jeffrey nanofluid with newtonian heating. J Aerosp Eng 2016;29(3):1–9.
[41] Dalir N, Dehsara M, Salman Nourazar S. Entropy analysis for magnetohydrodynamic flow and heat transfer of a jeffrey nanofluid over a stretching sheet. Energy 2015;79:351–62.
[42] Sandeep N, Sulochana C, Isaac Lare A. Stagnation-point flow of a Jeffrey nanofluid over a stretching surface with induced magnetic field and chemical reaction. Int J Eng Res Africa 2015;20:93–111.
[43] Hayat T, Asad S, Alsaedi A. Analysis for flow of Jeffrey fluid with nanoparticles. Chin Phys B 2015;24(4):1–8.
[44] Nadeem S, Saleem S. An optimized study of mixed convection flow of a rotating Jeffrey nanofluid on a rotating vertical cone. J Thermophys Heat Transf 2015;12:1–8.
[45] Raju CSK, Jayachandra Babu M, Sandeep N. Chemically reacting radiative MHD Jeffrey nanofluid flow over a cone in porous medium. Int J Eng Res Africa 2015;19:75–90.
[46] El-dabe NTM, Moatimid GM, Hassan MA, Mostapha DR. Analytical solution of the peristaltic flow of a Jeffrey nanofluid in a tapered artery with mild stenosis and slip condition. Int J Innov Appl Stud 2015;12(1):1–32.
[47] Akbar NS, Nadeem S, Noor NFM. Free convective MHD peristaltic flow of a Jeffrey nanofluid with convective surface boundary condition: a biomedicine-nano model. Curr Nanosci 2014;10:432–40.
[48] Akbara NS, Nadeemb S. Mixed convective magnetohydrodynamic peristaltic flow of a Jeffrey nanofluid with Newtonian heating. Z Naturforsch 2013;68:433–41.

[49] Hayat T, Shafique M, Tanveer A, Alsaedi A. Radiative peristaltic flow of Jeffrey nanofluid with slip conditions and joule heating. PLoS ONE 2016;11(2):1–11.
[50] Salah F, Abdul Aziz Z, Chuan Ching DL. MHD accelerated flow of second grade fluid in a porous medium and rotating frame. IAENG Int J Appl Math 2013;43(3):1–8.
[51] Khan M. Partial slip effects on the oscillatory flows of a fractional Jeffrey fluid in a porous medium. J Porous Media 2007;10(5):473–87.
[52] Hayat T, Khan M, Fakhar K, Amin N. Oscillatory rotating flows of a fractional Jeffrey fluid filling a porous space. J Porous Media 2010;13(1):29–38.
[53] Gul A, Khan I, Shafie S, Khalid A, Khan A. Heat transfer in MHD mixed convection flow of a ferrofluid along a vertical channel. PLoS ONE 2015;10(11):1–14.
[54] Ghara N, Das S, Maji SL, Jana RN. Effect of radiation on MHD free convection flow past an impulsively moving vertical plate with ramped wall temperature. Am J Sci Ind Res 2012;3(6):376–86.
[55] Kakaç S, Pramuanjaroenkij A. Review of convective heat transfer enhancement with nanofluids. Int J Heat Mass Transf 2009;52:3187–96.
[56] Loganathan P, Nirmal Chand P, Ganesan P. Radiation effects on an unsteady natural convective flow of a nanofluid past an infinite vertical plate. Nano Br Rep Rev 2013;8(1):1–10.
[57] Qasim M, Khan ZH, Khan WA, Ali Shah I. MHD boundary layer slip flow and heat transfer of ferrofluid along a stretching cylinder with prescribed heat flux. PLoS ONE 2014;9(1):1–6.
[58] Khan ZH, Khan WA, Qasim M, Shah IA. MHD stagnation point ferrofluid flow and heat transfer toward a stretching sheet. IEEE Trans Nanotechnol 2014;13(1):35–40.
[59] Turkyilmazoglu M. Unsteady convection flow of some nanofluids past a moving vertical flat plate with heat transfer. J Heat Transfer 2013;136:1–7.
[60] Turkyilmazoglu M, Pop I. Heat and mass transfer of unsteady natural convection flow of some nanofluids past a vertical infinite flat plate with radiation effect. Int J Heat Mass Transf 2013;59:167–71.
[61] Pantokratoras A, Fang T. Sakiadis flow with nonlinear rosseland thermal radiation. Phys Scr 2013;87:1–5.
[62] Cortell R. Fluid flow and radiative nonlinear heat transfer over a stretching sheet. J King Saud Univ 2014;26:161–7.
[63] Ahmed N, Khan U, Mohyud-din ST. Influence of nonlinear thermal radiation on the viscous flow through a deformable asymmetric porous channel: a numerical study. J Mol Liq 2017;225:167–73.
[64] Khan I. A note on exact solutions for the unsteady free convection flow of a Jeffrey fluid. Z Naturforsch 2015;70(6):272–84.
[65] Samiulhaq A, Khan I, Ali F, Shafie S. Free convection flow of a second grade fluid with ramped wall temperature. Heat Transf Res 2014;45(7):579–88.
[66] Hayat T, Awais M, Asghar S, Hendi AA. Analytic solution for the magnetohydrodynamic rotating flow of Jeffrey fluid in a channel. J Fluids Eng 2011;133:1–7.
[67] Sandeep N, Sugunamma V, Mohan Krishna P. Effects of radiation on an unsteady natural convective flow of a Eg-nimonic 80a nanofluid past an infinite vertical plate. Adv Phys Theor Appl 2013;23:36–43.
[68] Khalid A, Khan I, Shafie S. Exact solutions for free convection flow of nanofluids with ramped wall temperature. Eur Phys J Plus 2015;130(57):1–14.
[69] Mojumder S, Saha S, Saha S, Mamun MAH. Effect of magnetic field on natural convection in a C-shaped cavity filled with ferrofluid. Procedia Eng 2015;105:96–104.